TAMPERE UNIVERSITY OF TECHNOLOGY

JAROLD A. GONZÁLEZ SOSA

THE EFFECT OF ELF ELECTRIC FIELDS ON IMPLANTABLE CARDIOVERTER DEFIBRILLATORS

Master's thesis

ABSTRACT

Through research and technological advances, modern society has developed a variety of implantable devices that helps to optimize human's life quality. One of these devices is the implantable cardioverter defibrillator (ICD). Our unit, ERP Environmental Health, in previous investigations has found that, in some cases, the ICD receives certain disturbances under the power lines. Therefore it is important to study the degree of immunity that implants have against electromagnetic fields, because even small interference that result from EMF exposure could deliver a major public health impact.

The aim of this master thesis is to study the effect of extremely low frequency (ELF) non-uniform electric fields on implantable cardioverter defibrillators (ICD). This test was conducted in the laboratory of High Voltage Technology, University of Tampere, in a controlled climate room. The experiment consisted in introducing the ICD in the interior of a Human-Shaped phantom which was filled with a saline solution to emulate the conductivity within the human body; the phantom was subsequently exposed to an electric field between two parallel plates.

Following the experiment, we created a three-dimensional model of the electromagnetic fields generated by a phantom. This allowed us to corroborate the experiment and calculate quantities that it was impossible to obtain physically, such equipotential lines and the electric field lines between the parallel plates. We also calculated the total induced current and compared with experimental results, obtaining in a worse case a mean relative error of 10.53%, which suggests that our calculations are in agreement with the experimental result. However, an additional comprehensive study is needed to obtain more conclusive results.

PREFACE

I would like to show my gratitude to all those who in one way or another, have contributed to the realization of this master thesis.

I acknowledge Professor Leena Korpinen, who took me in and made me feel welcome in her research group and gave me the opportunity to carry out my master thesis. Also I want to give thanks to Professor Lauri Kettunen for his help and great advice.

The patience and invaluable help to my research from Professor Hiroo Tarao was much appreciated.

I want to acknowledge Dr. Kari Lahti, Head of the High Voltage Laboratory, for his assistance during the experimental part of this project.

Also thanks to my work colleagues Markus Wirta and Tero Haapala for their support throughout this project, and especially in my early days here in Finland.

I could not have been where I am today without my family, who I have to give thanks for their love and support unconditionally. In the same note, I also acknowledge my girlfriend, for walking by my side down this road.

TABLE OF CONTENTS

LIST OF SYMBOLS

ELF	Extremely Low Frequency
ICD	Implantable Cardioverter Defibrillator
PM	Pacemaker
SA	Sinoatrial
VF	Ventricular fibrillation
VT	Ventricular tachycardia
PRM	Programmer Record Monitor
ECG	Electrocardiography
EGM	Electrogram
CAN	ICD housing
EMI	Electromagnetic interference
BVP	Boundary Value Problem

1. INTRODUCTION

Modern technology has helped develop a wide variety of devices that help counteract the physical anomalies of the human being. These may include cochlear implants, retinal implants, implantable artificial limbs, bioelectronics noses, spinal cord stimulators, implantable insulin pumps, implantable cardioverter defibrillators (ICD) or pacemakers (PM) [1–9].

The number of people who need to use these dipositive has increased rapidly. For example in the U.S. the number of people with heart disease who require cardiac device implantation has reached 800,000 each year [10]. Conflictingly, there are also many devices which can produce electric and magnetic fields. Correspondingly, it is reasonable to ask if it is possible that some devices can influence in medical implants.

The focus of this master thesis is on ICD since extremely low frequency (ELF) electric field can cause malfunctions or disturbances in implantable defibrillators as reported in previous research [9]. These disturbances can cause two equal dangerous situations. The first is that the ICD detects ventricular fibrillation and erroneously applied an electric shock at the patient's heart. The second is that the ICD does not detect when the heart is fibrillating and inhibit shock therapy, which could cause death. For this reason the aim of this master thesis is to study the degree of immunity that implants have against electromagnetic fields as even small interference that results from EMF exposure could have a major public health impact.

Usually, when people are exposed to ELF electric and magnetic fields, this result in the induction of internal electric fields and currents within the body. If the internal currents are relatively high, the human can experience nerve tissue stimulation [11], and this can also influence the medical implant. The mechanism of interaction between the internal currents and the implants is however still unclear. It is therefore of great importance to study the degree of immunity that implants having against electric and magnetic fields.

The magnitude of internal electric field induced from external electric or magnetic fields in the human body can be estimated by calculations. Different physical models [12] and anatomically correct computational models [13–16] have been developed to simulate the human body, in order to calculate internal current densities or internal electric fields.

Nowadays, calculations are performed by using numerical methods and software systems. In addition, the computational methods can be used to evaluate the currents and electric fields induced inside the human body by such exposures, and it can lead to the subsequent assessment of disturbances in the medical implants. This topic has previously been published e.g. by researchers [17].

2. THE HEART

The first successful definition of this organ was formulated by William Harvey in 1628, describing it as a muscular "pump", thus dismissing the traditional belief that the heart was the source of body heat [18] . Certainly this definition has been refined over the years. As science has allowed man to achieve better knowledge of how the heart works, it is currently defined as "The muscular organ that acts as a hydraulic pump in the cardiovascular circuit" [19], [20].

2.1   Anatomy of the heart

2.1.1   Location of the heart

The heart is located in the thorax, behind the sternum and anterior to the oesophagus, the aorta and the spine. On either side of it, are positioned the lungs. One third of the heart is situated to the right of the body midline and two thirds to the left (Figure 2.1).

Figure 2.1. Heart inside the human body. Image courtesy of http://www.jano.es website belongs to Elsevier.

2.1.2. External morphology

The heart is a hollow muscular organ, shaped like an inverted cone with the tip (apex) directed to the left. It is contained within the pericardium. The main function of the heart is to pump blood through the blood vessels to provide the body tissues with essential gasses and nutrients. It receives blood from the venous trunks and expels it into the arterial system.

It is generally considered that the heart is similar to the size of the person's fist. The size and weight of this organ varies considerably with age, sex, height, epicardial fat and general nutritional status. Thus, it is considered that the heart weighs 0.45% of body weight in men and 0.40% of body weight in women, so that in an average-sized adult the heart weight ranges between 250-350 g in men and between 200-300 g in women. When it comes to professional athletes, usually the heart shows a physiological increase in weight morphology [21].

The inside of the heart consists of four chambers: two on the right side and two on the left, hence it is common to speak in terms of "right heart" and "left heart". The cavities located at the top are termed atria, and those situated in the lower part are ventricles. Under normal conditions, the right cavities are separated from the left by a muscular wall called the interatrial septum, which separates the two atria and the interventricular septum that divides both ventricles (see Figure 2.2).

The organ is formed by the heart wall, chambers and arteries, veins and nerves that are responsible for its irrigation and innervations.

The atria (right and left) are of a muscular nature. The right atrium connects to the right ventricle via the atrioventricular orifice, the opening and closing of which is regulated by the tricuspid valve. The right atrium is supplied by the superior and inferior cava veins, which collect the de-oxygenated blood running throughout the body. The left atrium is connected to the left ventricle by means of another atrioventricular orifice, regulated by the mitral (bicuspid) valve. It is supplied by the four pulmonary veins, which carry arterial (oxygenated) blood from the lungs to the heart [22].

The ventricles are the lower chambers of the heart, with thick walls and whose contractions make effective the impelling action of the heart. Both cavities are separated by a muscular wall, the interventricular septum. The right ventricle expels via the pulmonary artery through a semi lunar (pulmonary) valve, which prevents the reflux of arterial blood into the ventricle during relaxation phase. It is responsible for carrying venous blood to the lungs (the pulmonary system of the body). The left ventricle has greater capacity than the right and its muscular walls are thicker. It expels to the circulatory system of the body via the aorta through a semi lunar (aortic) valve, which has similar characteristics to the pulmonary valve. This prevents the reflux of arterial blood into the ventricle during the relaxation phase [23].

The fibrous skeleton of the heart is formed by the valve rings (atrioventricular and sigmoid) which give extensions and form the atrioventricular septum (upper) and inter-ventricular (bottom). The valves work rhythmically, allowing blood to move through the chambers of the heart in only one direction, therefore preventing the passage of blood in the opposite direction.
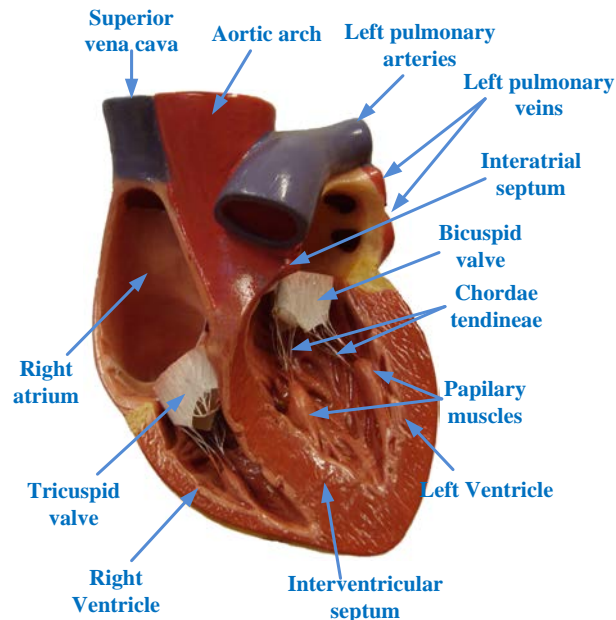
Figure 2.2. *Cross section of heart [18].*

2.2. Physiology of the heart

2.2.1. The heart muscle

The ceaseless activity of the heart depends essentially on a number of specific properties of the myocardium [24] ,which can be summarized in the following five principles:

1. **Automatism:** The ability to generate its own impulses.

2. **Conductivity:** The ability to conduct nerve impulses produced by the heart without loss of power/strength.

3. **Excitability:** An ability to respond to any physical, chemical, or electrical stimuli, generating a trans-membrane action potential.

4. **Contractility:** Responds to stimuli by a contraction which is a mechanical phenomenon is manifested by an inotropic action potential.

5. **Refractoriness:** Relating to the time interval in which the normal cardiac impulse cannot be re-energized prior to discharge, in an already excited part of the heart muscle.

2.2.2. Electrophysiological properties of the heart

Each heartbeat is controlled by electrical impulses which travel through the heart and is the result of a complex set of precise and coordinated events that interrelatedly occur both inside and outside the heart. The opening and closing of valves corresponds synchronously with the movements of contraction (systole) and relaxation (diastole) of the different chambers previously mentioned.

The conduction system plays a central role in the maintenance of the heart rhythm, and in the coordination of the muscle activity of the hearts chambers. The system is made up of specialized muscle fibres that initiate the process of conduction and the subsequent contraction of cardiac muscle fibres in the walls of the atria and ventricles.

This system consists of:

- Sinus (sinoatrial) Node: The natural pacemaker of the heart. Located below the insertion of the superior vena cava in the posterior wall of the right atrium.

- Atrioventricular Node: This is a small mass of specialized myocardial cells and located in the right atrium on the interatrial septum above the tricuspid valve.

- Atrioventricular Bundle of His: It originates in the atrioventricular node and flows downward through the membranous interventricular septum. It divides into two branches (the left and right bundle branches) which in turn subdivide to innervate all areas of the ventricles by means of the Purkinje fibres.

The depolarization and polarization of the sinoatrial (SA) node and other electrical system elements produce a marked pattern of changes in voltage that can be measured and recorded through electrodes placed on the skin. This graphic recording of the electrical potential generated by the heart is called an electrocardiogram or ECG, and is a diagnostic tool for the evaluation of heart function [25].

2.3. Electrocardiography

2.3.1. Electrocardiogram

Some authors considered that the standard ECG is a graphic transcription of five waves, see Figure 2.3. Those of slow course are called P and T waves; and for the fast course deflections: Q, R and S. These waves are shown always in the same order in the standard ECG. Exceptionally there is a 6th wave, called U, most visible in the right precordial leads. The wave generated by each heartbeat is reflected in the ECG as indicated in the figure on the left.
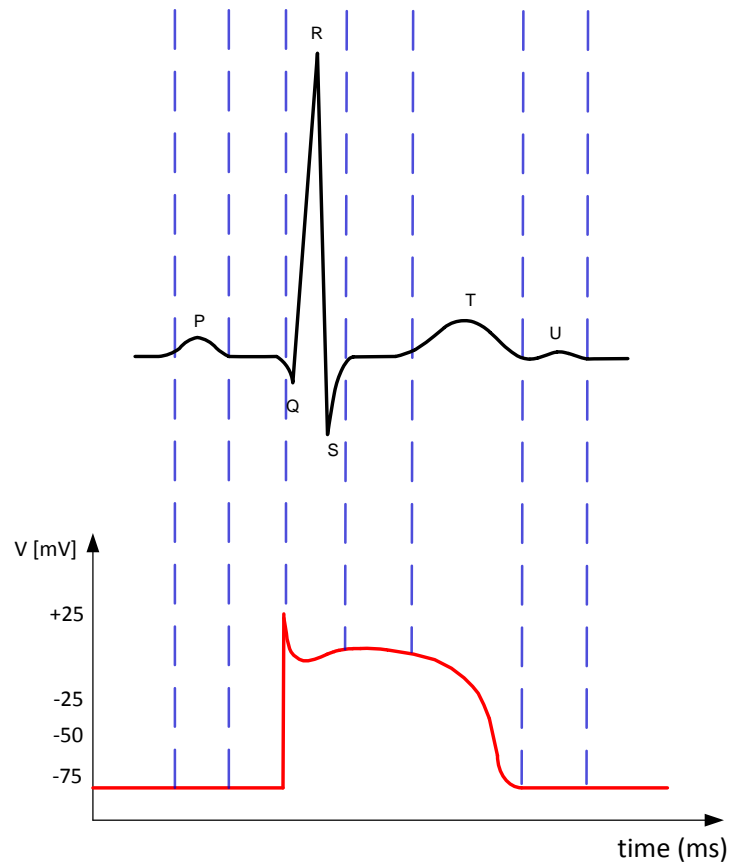
Figure 2.3. *Temporal relationships between the electrocardiogram (up) and a ventricular action potential (down).*

2.3.2. Heart rhythm disturbances

Any irregularity in the process of generation and conduction of electrical signals above mentioned causes a heart rhythm disorder or arrhythmia. In general, rhythm disturbances are due to two types of processes: abnormal electrical impulse formation or conduction abnormalities of the pulse [18], [19], [23]. However, the existence of irregular heartbeat or palpitations may be harmless and do not necessarily require medical attention. There are several ways to classify cardiac arrhythmias. One of the most used and simplest is the heart rate classification. The heart beats normally on a range from 60-100 beats/min (beats/min). If the heart rate is less than 60 beats/min, is called bradycardia; whereas if we exceed 100 beats/min it is called tachycardia. It is also often classified according to the mechanism of the arrhythmia and where it originates, see Appendix I.

The most lethal tachyarrhythmias are the ventricular tachycardia (VT) and the ventricular fibrillation (VF). Due to this, patients at high risk of arrhythmic episodes of VT or VF are indicated to use the automatic implantable defibrillator (ICD). The following chapter explains the basic concepts associated with this device.

3. IMPLANTABLE CARDIOVERTER DEFIBRILLA-TOR

The implantable cardioverter defibrillator (ICD) is the device used to prevent sudden death. The ICD uses electrical pulses or "shock" to control arrhythmias, especially those that cause this type of death. In the beginning was implanted in the abdomen because they were much larger and heavier, but today, their small size and light weight allow it to be implanted in the chest Figure 3.1. This will reduce the long term complications related to the leads [26].

Figure 3.1. ICD Model V-186HV3. St Jude Medical.

Since Dr. Michael Mirowski published his work in 1970, there have been many advances in the ICD technology. Mainly the functionality, reliability and versatility of the devices, has improved and has simplified, increasing patient satisfaction [27], [28]. There are many reasons for the achievement: electrophysiology, electronics, materials science, chemistry and computer science.

3.1. Hardware of the ICD

Current systems for the treatment of arrhythmias based on ICD are composed of three hardware components [29–33]:

- The programmer recorders monitor (PRM).
- The implantable cardioverter defibrillator.
- The intracavitary electrode system.

The ICD and the electrodes are the components implanted in the patient, while the PRM is an external device that provides a communication link through which the electrophysiologist can access non-invasively to the ICD software. The implantable cardioverter defibrillator is hermetically sealed in a biocompatible casing (CAN) that houses the batteries, capacitors, communication systems for defibrillation, pacing, heart rate monitoring and telemetry control system, the microprocessor and memory systems. Finally, the intracavitary electrode systems provide an interface between the physical and electrical heart and the ICD to cardiac activity monitoring and administration of electrical therapy.

Electrode systems are connected to the ICD via a wired internally structure, which provides the electrical path between them and gives mechanical support to the electrode system, when it is situated in the cardiovascular anatomy.

3.2.   The programmer remote monitor

The PRM is an external device that provides a bidirectional communication channel with the ICD implanted in the patient [28], see Figure 3.2. It is, therefore, the interface between the electrophysiologist and the ICD. Its main functions are: access data of the implants, convert it to a format readable by the electrophysiologist and program the ICD. The main data can be recovered by the PRM include EGM stored or recorded in real time, the patient's treatment history and status of the battery. Both the defibrillator as the PRM sends the encrypted information to detect these errors and reject the command. These codes are exposed to prevent intrusion by non-physicians, but recently have been shown not to be sufficiently safe from malicious attacks [34].

The internal components of the device vary from manufacturer to manufacturer, but generally consist of:

- A central processing unit.
- A data input device of the user.
- A monitor (if the screen is touch, may be the user input).
- One printer.
- An entry to electrocardiographic leads.
- A communications unit based on telemetry.

Figure 3.2. Zoom Latitude Programmer Boston Scientific. PRM used for the experiments.

Futher details on this can be found in U.S. Patent 7, 103, 414 B1 [35], which shows a block diagram of most of its components.

3.3.   The implantable cardioverter defibrillator

The implantable cardioverter defibrillator is implanted and autonomous component. This is encapsulated in hermetically sealed titanium housing, see Figure 3.3. The titanium is the material used in these implants because it is strong, biocompatible and has low density [6].
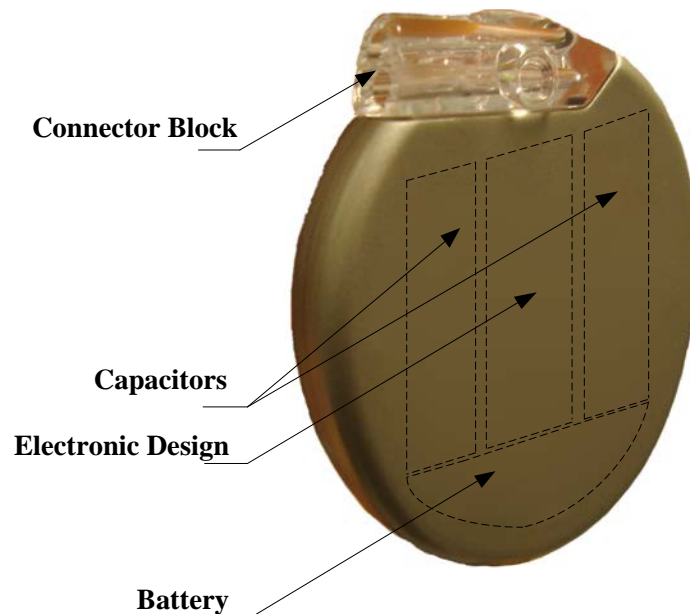
Figure 3.3 Components of a generic ICD. As you can see the capacitors are responsible for a large percentage of the size of the device, based on [31], [33], [36].

CAN protects the battery and the electrical circuitry of the corrosion of body fluids, also forms a Faraday cage which prevents the direct interference of external electromagnetic interference (EMI).

The ICD is generally composed of the following interfaces: Telemetry, sense input, high-voltage output, pace output, audio transducer, as reported [29], [36], [37].

3.3.1. Telemetry Interface

When the electrophysiological want to communicate with the implant, it should make this communication by placing the programming wand (PRM telemetry system), see Figure 3.4, a distance of 10 cm at most, because it must close the circuit through a reed. Communication through the programming wand allows the electrophysiologist to vary one or more parameters of the ICD, such as tachycardia and bradycardia therapy, enable the immediate transmission of the electrocardiogram, charge the capacitors to the maximum voltage, apply shock therapy, etc.
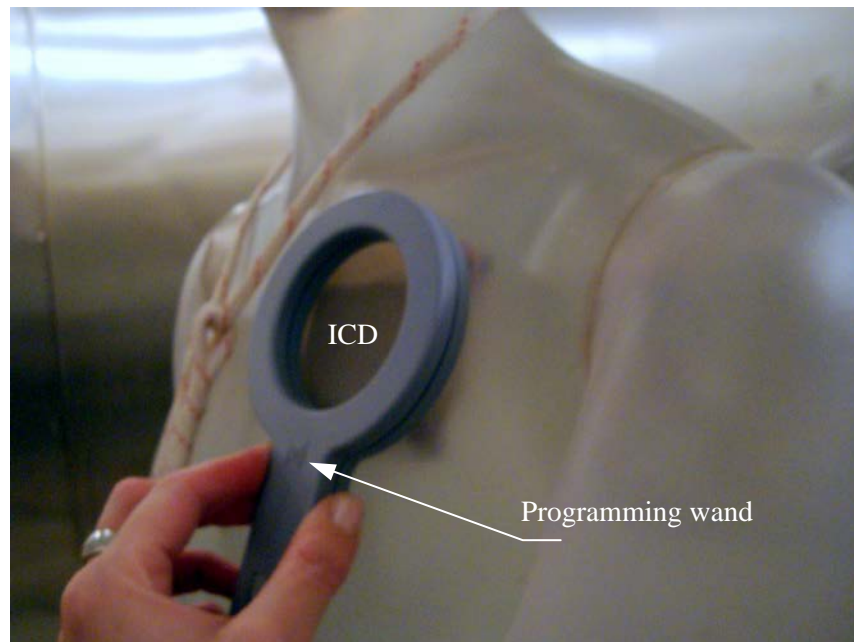
Figure 3.4. *Establishing connection with the ICD by the programming wand.*

Data transmission and communication speed vary from one manufacturer to another. As mentioned above, this communication is done through codes to check if the message sent is correct and to some extent corrects errors due to data transmission. If you want more information, about the operation of the telemetry interface can be found in the U.S. Patent 7,103,414 B1 [38], which is a detailed explanation of the circuit that implements it.

3.3.2.   Sense input Interface

The signal obtained from the electrodes is analog, see Figure 3.6, which is not ideal for monitoring the state of the heart, so this signal is converted to a digital signal to obtain a binary signal (1.0), see Figure 3.7. The following block diagram explains the main components of this signal conditioning [30].
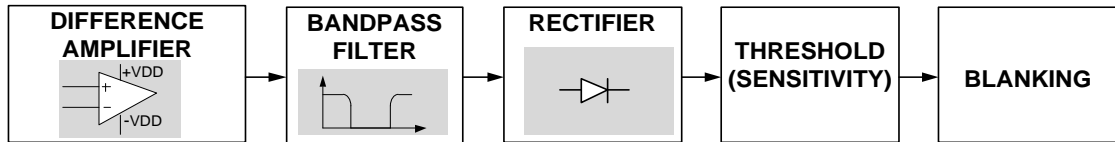
Figure 3.5. Simplified block diagram of the sense input interface.

The signal coming from the electrodes has the following form:
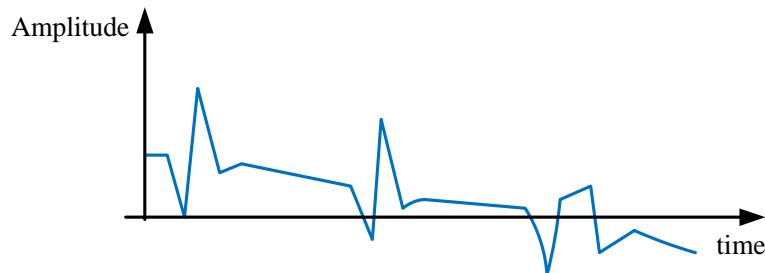
Figure 3.6. Sketch of the signal from the electrodes [30].

Differential Amplifier: The amplifier allows rapid recovery after stimulation or defibrillation shocks. It also rejected large DC offsets due to the polarization of the electrode and the common mode noise applied to the two inputs [30].

Bandpass filter: Removes or attenuate the signals appearing at low frequencies such as the T waves and the same measure eliminates or attenuates high frequency signals such as myopotentials. Another important function that has this filter is to remove the majority of electromagnetic interference (EMI) [29].

Rectifier: The full-wave rectifier can reverse any negative deflection signal for the detection threshold of the R wave is not affected by the polarity, which may vary for different rhythms [36].

Threshold (Sensitivity): It acts as a comparator which compares the rectified signal with the threshold voltage and senses the R wave when it exceeds this threshold, when the R wave is detected, it generates a pulse [36].

Blanking: The purpose of this block is to sense every depolarization only once, it should be noted that the "blanking period" cannot be used to prevent oversensing of the T wave because typical QT intervals or RT are higher than shorter RR during ventricular fibrillation. The signal after the blanking block is show in the Figure 3.7.
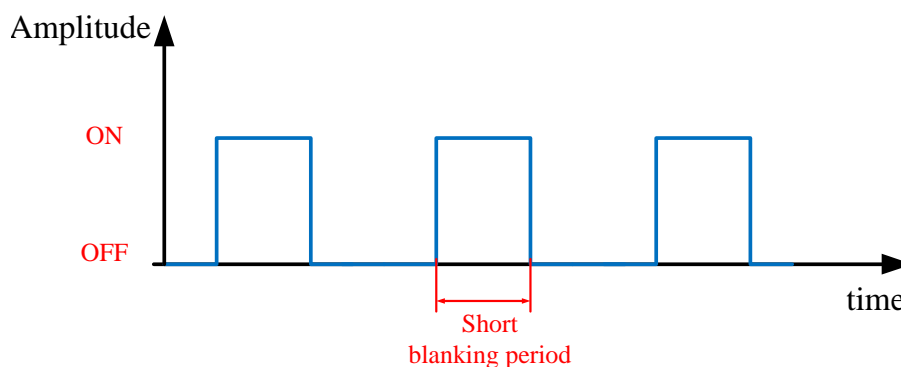
Figure 3.7. Sketch of the signal after the rectifier blanking block [29].

3.3.3. High-voltage output interface

This interface is the most important and the reason for the ICD, consists of the charging circuit, two capacitors of high capacity and output switches as reported [8], [29], [31], [33]. After the detection of a tachycardia and initiation by the microcomputer of the ICD charging high voltage capacitors, this converts the battery voltage (3.2V BOL[3] [30]) into between 800V and 750V in about 10 s. Subsequently when the microcomputer decides to apply the shock to the patient, activated the output switches. These actions can be controlled by the microcomputer or a digital circuit built for this purpose [29].

3.3.3.1 Pace output interface

This interface is responsible for providing "the pacing therapy for bradycardia or tachycardia" depending on the case. The electronic device responsible for the detection of the tachyarrhythmia and delivery of the shock is the microcomputer, although, the digital circuit can be custom ordered sequence to provide an antiarrhythmic the microprocessor is at least starting this activity [29]. The microprocessor controller may be through the telemetry interface, allowing activating or deactivating the bradycardia pacing as well as control of the parameters: rate, pulse width, etc.

The microcomputer provides support components such as RAM (Random Access Memory) is memory is additional space for the program is running, the storage of operating parameters and storing electrogram (EGM). Also is this the ROM (Read Only Memory) is a volatile memory for system startup and program space.

---

[3] BOL Beginning of life: is the voltage at the battery open circuit when it has the maximum charged

The block diagram shown in Figure 3.8 summarizes each of the interfaces within the implantable defibrillator.
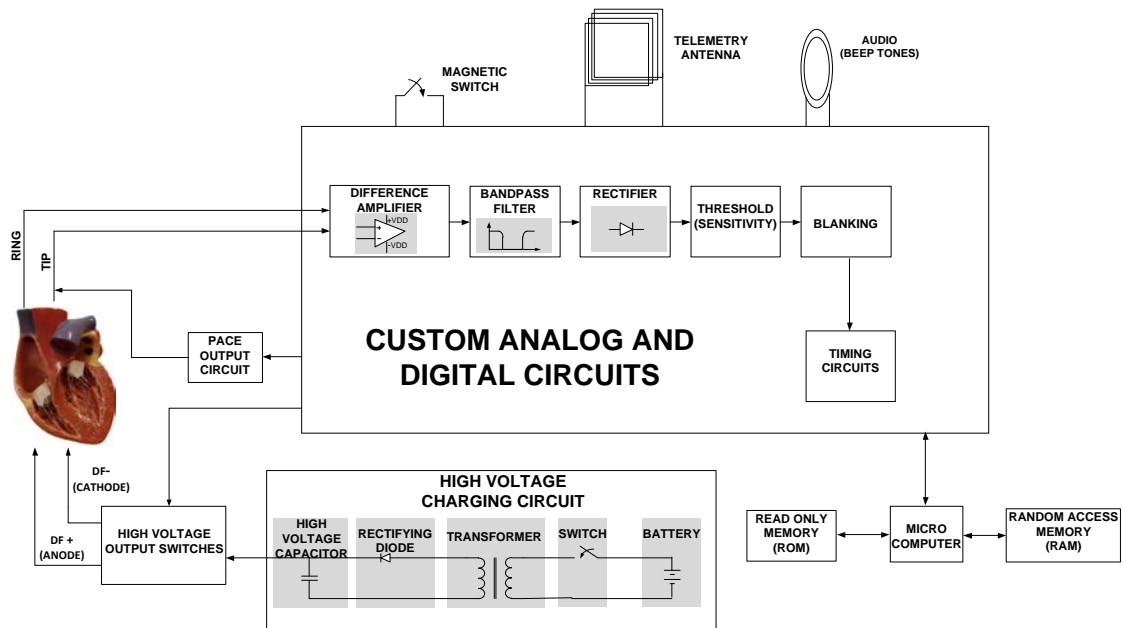
Figure 3.8. The complete block diagram of the internal system of the ICD. Information based on [29], [30], [35], [36], [38].

3.4. Lead and electrodes. Technical aspects

The electrodes provide the electrical interface between the heart, on the one hand, and the ICD on the other. The derivation provides an electrical path between the two and additionally constitutes a rigid guide to direct the electrodes toward its final location, which provides a stable mechanical support.

Depending on their role in the monitoring and management functions of electrical therapies, the typical characteristics such as surface electrodes and anatomical location vary. The electrodes typical basic functions are as follows in the Figure 3.9.
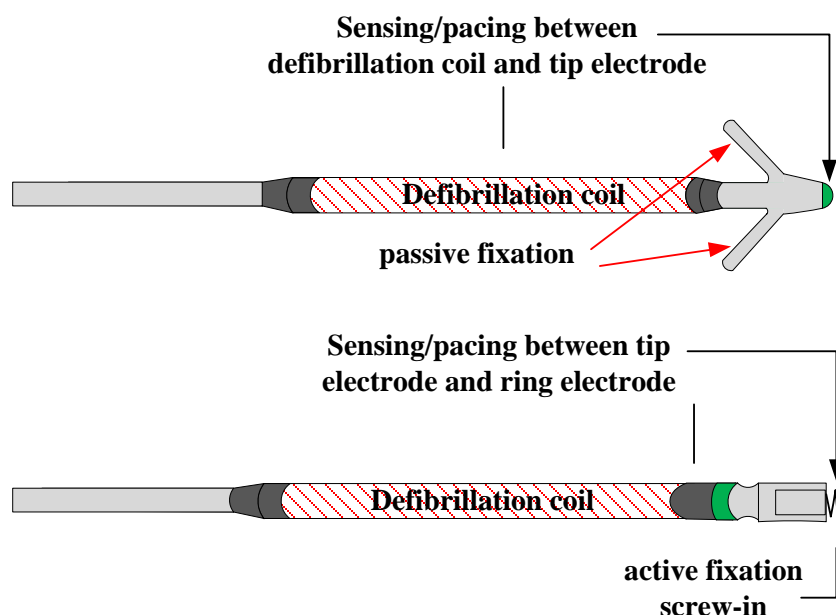
Figure 3.9. *Final section of a lead, in the top of the figure shows a configuration consisting of a tip electrode and an electrode coil with a passive fixation. While at the bottom of the figure shows a configuration consisting of an electrode tip and a ring electrode with an active fixation [29].*

- **Tip:** the most distal electrodes. Its surface is small and is located at the apex of the RV [36].
- **Ring:** It consists in the lead a few millimeters from the tip electrode are of small area [38].
- **Proximal coil:** It is located usually in the superior vena cava and has large surface area [36].
- **Distal coil:** It is located in the right ventricle near the electrode tip and has a large surface [29].

The combinations of two or more electrodes provide electrical pathways for the functions of monitoring and management of electrical therapies. Lower surface electrodes are involved in the stimulation and monitoring functions while the larger surface used in the functions of monitoring and defibrillation [36].

Depending on the combination of electrodes used in the monitoring functions, it is customary to distinguish between two configurations which provide different nature EGM [39], [40].

- **Bipolar:** also called the sensing configuration. Similar to the electrode systems of first-generation ICDs, this configuration consists of electrodes physical proximity located close of the myocardial wall. The electrodes can be tip, ring and distal coil. The bipolar configuration can be of two types [29]:

- **True bipolar system.** From tip to ring. This configuration is also involved in pacemaker stimulation, and participating in monitoring heart activity [36].

- **Integrated bipolar system.** From tip to distal coil. It is so named because the distal coil integrates the functions of monitoring, pacing stimulation along the electrode tip, and defibrillation with the housing of the implant and the proximal coil in superior vena cava [36].

- **Unipolar:** Also called the pseudo-monopolar configuration, use the distal coil and the housing of the implant for monitoring the heart activity and administration of electrical therapy [29].

Detection algorithms use essentially the EGM provided by the bipolar configurations. In each model of transvenous lead, usually only implemented a bipolar configuration. The dedicated bipolar are the best option for monitoring and pacing stimulation, although, because the distal coil is located farther from the apex, this configuration has a greater pull-back during defibrillation [41]. This problem can be overcome by implementing an integrated bipolar configuration dispenses with the ring electrode so that the distal coil is located closer to the apex. However, there have been delays in redetection of arrhythmias when using integrated bipolar configurations [36].

4. THE ELECTROMAGNETIC FIELDS

4.1. Electromagnetic theory

Electromagnetic fields are specified by Maxwell's equations and the constitutive relations [43]. Typically, one sets a boundary value problem (BVP) from which some boundary conditions. Numerically BVP are often solved with the technique called finite element methods (FEM).

4.1.1. Gauss's Law for the electric field

Gauss's law states that regardless of the shape of the charge distribution that produces the field, the electric field flux through a closed surface is proportional to the net charge contained in the internal volume [44]. It is important to note that Gauss's law involves the idea that the definition of charges does not depend on the scale.

Gauss's law is expressed in its integral form as follows [45]:

$$\int_{\partial V} \mathbf{D} \cdot \mathbf{n} \, da = \int_{\partial V} \rho \, dv \qquad \forall V, \qquad (4.1)$$

where: **D**   the electric displacement,

ρ Electric charge density,

V Volume containing the electric charge.

Gauss's law can also be expressed in differential form [43]:

$$\nabla \cdot \mathbf{D} = \rho. \qquad (4.2)$$
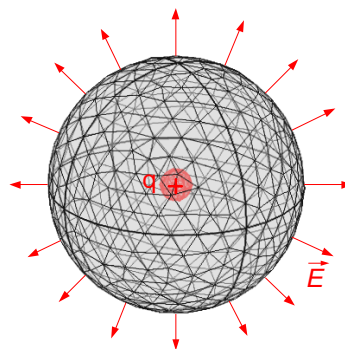
Figure 4.1. *Electrical flow of a positive point charge through a closed surface.*

4.1.2. Gauss's Law for the magnetic field

Experimentally we reached the result that the magnetic fields, unlike electric fields do not begin and end at different charges. The law of Biot and Savart allows us to easily prove Gauss's law for the magnetic field, this law states that on a closed surface, regardless of which, we will not be able to lock a source (source) or drain (drain) field, demonstrating the absence of magnetic charge [42], [45]:

Surface: Magnetic flux density norm (T) Arrow Surface: Magnetic flux density
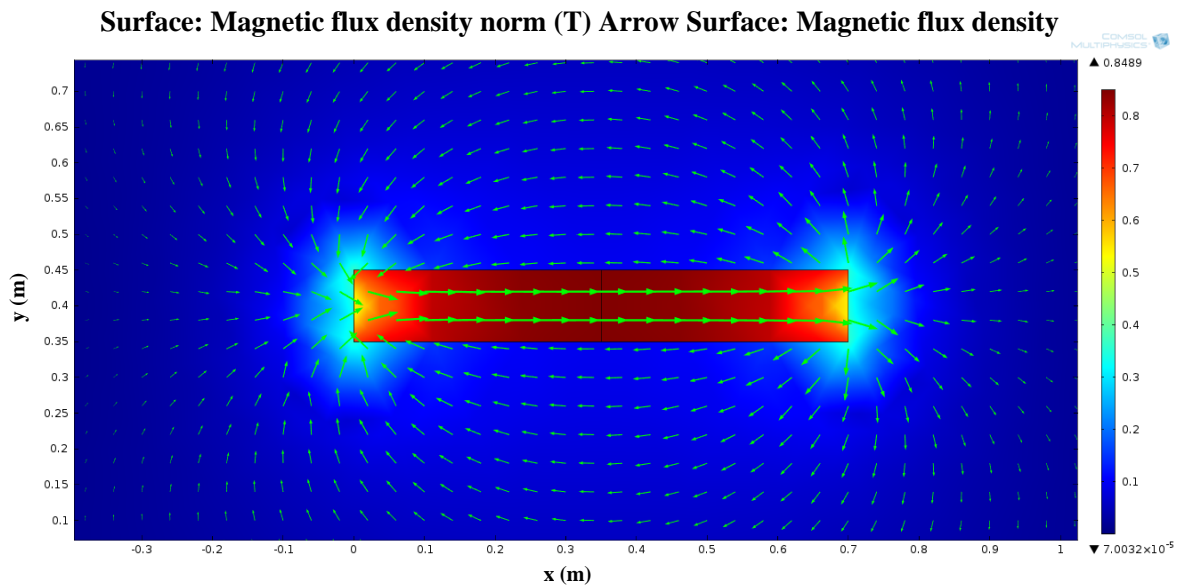
Figure 4.2. *2D simulation on the plane (XY). All magnetic field lines coming into a closed surface leave again.*

$$\int_{\partial V} \mathbf{B} \cdot \mathbf{n} \, da = 0 \qquad \forall V, \qquad (4.3)$$

where: $\mathbf{B}$ Magnetic flux density,

V Volume.

In differential form is represented as follows [44]:

$$\nabla \cdot \mathbf{B} = 0. \qquad (4.4)$$

4.1.3. Faraday's Law

Faraday's law states that the electric field is defined the same way for all observers [42]. It is about electromagnetic induction, which causes an electromotive force.

$$\int_{\partial S} \mathbf{E} \cdot d\mathbf{l} = -\frac{d}{dt} \int_{S} \mathbf{B} \cdot \mathbf{n} da \qquad \forall S, \qquad (4.5)$$

The electromotive force ξ is defined as [44]:

$$\xi = \int_{\partial S} \mathbf{E} \cdot d\mathbf{l}. \qquad (4.6)$$

If we make the limit of equation (4.6) when $S \to 0$ we can obtain the Faraday equation in differential form:

$$\nabla \times \mathbf{E} = -\frac{\partial \mathbf{B}}{\partial t}. \qquad (4.7)$$

4.1.4. Generalized Ampère's Law

The first law proposed by Ampere showed inconsistency with the principle of conservation of charge [42]. To resolve this inconsistency Maxwell introduced a term which today is known as displacement current. So the generalization of Ampère's law, known as Ampère-Maxwell, is presented below [44]:

$$\nabla \times \mathbf{H} = \left(\mathbf{J} + \frac{\partial \mathbf{D}}{\partial t} \right), \qquad (4.8)$$

where: $\mathbf{H}$ Magnetic field,

             $\mathbf{J}$ Current density,

             $\dfrac{\partial \mathbf{D}}{\partial t}$ Displacement current.

The term introduced by Maxwell has a great importance in electromagnetism and which predicts the existence of electromagnetic waves. If you look at the equations of Faraday and Ampère-Maxwell we see that the time-varying fields, once created by the currents and charges can sustain each other [44]. That is, a magnetic field varying, according to Faraday, creates an electric field, which in turn will also vary over time and according to Maxwell, it creates a magnetic field, whereupon the cycle generator is closed. Thus, the fields can exist without the need of charge or currents, and therefore, can propagate. This is the principle of propagation of electromagnetic waves, theoretically predicted by Maxwell and later demonstrated experimentally by Hertz [42].

A special case is when the electric field changes are negligible the equation (4.8) is simplified as shown in equation (4.9)

$$\nabla \times \mathbf{H} = \mathbf{J}. \tag{4.9}$$

Since the FEM technique used differential equations to find the solution to the boundary value problem, we present the Maxwell equations in compact and differential form on the Table 1.

Table 4.1 *Maxwell's Equations [42], [44], [45].*

Differential Form	Law of
$\nabla \times \mathbf{E} = -\dfrac{\partial \mathbf{B}}{\partial t}$	Faraday
$\nabla \times \mathbf{H} = (\mathbf{J} + \dfrac{\partial \mathbf{D}}{\partial t})$	Ampère-Maxwell
$\nabla \cdot \mathbf{D} = \rho$	Gauss's law for the electric fields
$\nabla \cdot \mathbf{B} = 0$	Gauss's law for magnetic field. No isolated magnetic charge.

4.2. Constitutive Relations

For a complete system of equations, we use the constitutive relations that describe the macroscopic properties of the medium [46–48]

$$\mathbf{D} = \epsilon \mathbf{E}, \tag{4.10}$$

$$\mathbf{B} = \mu \mathbf{H}, \tag{4.11}$$

$$\mathbf{J} = \sigma \mathbf{E}. \tag{4.12}$$

The same relations can also be given by [46]:

$$\mathbf{D} = \epsilon_0 \mathbf{E} + \mathbf{P}, \tag{4.13}$$

$$\mathbf{B} = \mu_0 (\mathbf{H} + \mathbf{M}), \tag{4.14}$$

$$\mathbf{J} = \sigma \mathbf{E}. \tag{4.15}$$

The polarization **P** and magnetization **M** described how the material is polarized and magnetized at a specific point.

4.3. Potentials

As we want to form second order problems it is useful to express the problem in terms of electric scalar potential V and the magnetic vector potential $\mathbf{A}$ [42].

Since $\int_{\partial V} \mathbf{B} \cdot \mathbf{n}\, da = 0 \;\; \forall V$ then exist $\mathbf{A}$ such that

$$\mathbf{B} = \nabla \times \mathbf{A} \tag{4.16}$$

If we substitute this equation in (4.7) we get

$$\nabla \times \mathbf{E} + \frac{\partial}{\partial t} \nabla \times \mathbf{A} = \mathbf{0} \tag{4.17}$$

Assuming the continuity of the fields, we can interchange the order of the partial derivative and the curl, where we obtain

$$\nabla \times \left(\mathbf{E} + \frac{\partial \mathbf{A}}{\partial t} \right) = \mathbf{0} \tag{4.18}$$

Since the curl $\left(\mathbf{E} + \frac{\partial \mathbf{A}}{\partial t} \right)$ vanishes then [44]

$$\mathbf{E} = -\nabla V - \frac{\partial \mathbf{A}}{\partial t} \tag{4.19}$$

holds, for $\nabla \times \nabla V \equiv 0$.

4.4. Quasi-Static Approximation

A consequence of Maxwell's equations is that changes in time of currents and charges are not synchronized with the changes of the electromagnetic fields [42].

Electric fields are always delayed with respect to changes in the source due to the finite speed of propagation of electromagnetic waves [46]. If we assume that we can ignore this fact, it is possible to obtain the electromagnetic fields assuming that the field changes instantly with change in the charge distribution; this approach is known as "Quasi-Static Approximation". The approximation is valid provided that the variations in time are small and that the studied geometries are considerably smaller than the wavelength [49].

If we apply the law of conservation of change we get:

$$\nabla \cdot \mathbf{J} = 0. \tag{4.20}$$

Besides the displacement current $\partial \mathbf{D}/\partial t$ is negligible and can be removed from the Maxwell-Ampere equation. It is also eliminated the term $\partial \mathbf{A}/\partial t$ in equation (4.20) this simplifies said equation resulting in the following equation:

$$\mathbf{E} = -\nabla V.$$

(4.21)

4.4.1. Parallel Plates

An interesting case to study is two parallel plates case, since is the configuration will be used in the experiment. In this configuration the electric field is uniform and can be calculated using equation (4.22) in the central space bounded by two plates. As we move away from this central area and approach the edges, this equality no longer holds and loses the uniformity mentioned above [42]; appearing the ends effect, see Figure 4.3.

$$E = \frac{V}{d}$$

(4.22)
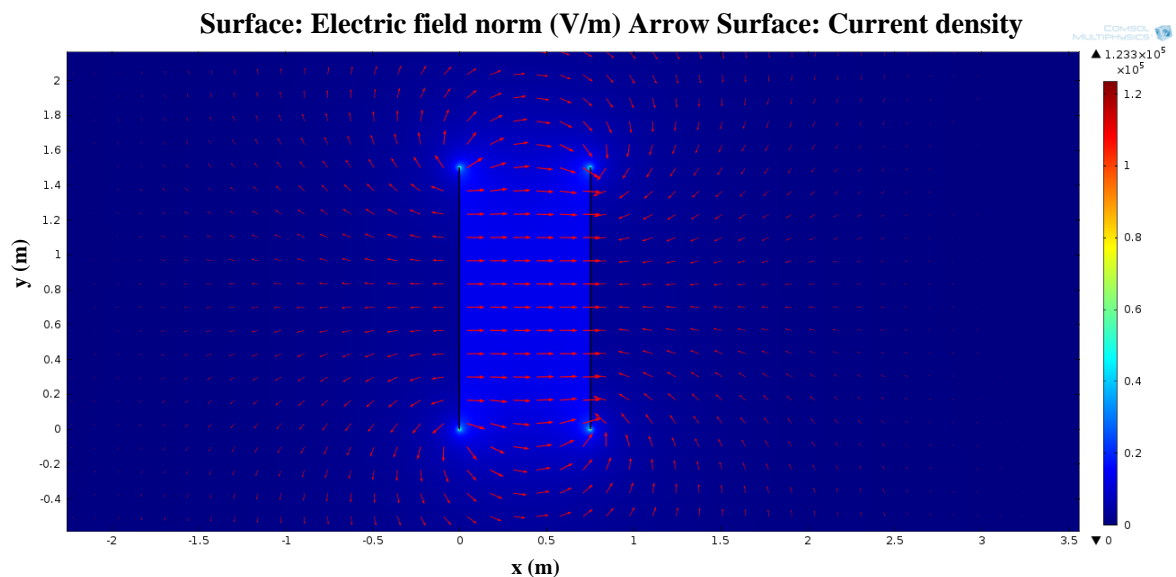
Figure 4.3. *Comsol Multiphysics simulation carried out in 2D (XY plane). Two parallel plates (1500 x 3) mm, where the legend representing the intensity of electric field and the arrows represent the current density.*

If we make a representation of the electric field as a function of position in the XY plane, the end effect can be observed at the four corners of the parallel plates, see Figure 4.4.
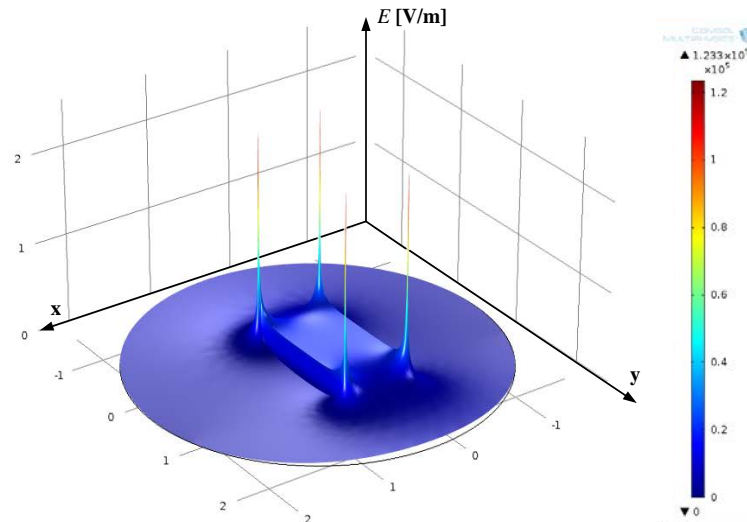
***Figure 4.4.** Representation of the electric field intensity as a function of position in the XY plane.*

4.5. Extremely low frequency (ELF) electric and magnetic fields

The extremely low frequency fields are defined so that their frequency is less than 300 Hz (f <300 Hz). At low frequency, the wavelength of the electromagnetic waves is the order of $\lambda = c/f = 3 \cdot 10^5 (\text{km/s})/300(\text{Hz}) = 1000$ km. In materials with electric and magnetic properties of living tissue, ELF field has a wavelength much larger than the size of the human body [50], allowing us to apply the quasi-static approximation. In that case, the electric and magnetic fields are decoupled. Furthermore, if we analyze the daily exposure to such fields it can be distinguish between two cases [51].

1. Exposure to low voltage and high current: in this case the field that predominates is the magnetic field. It decreases with distance and is very close to the source; the currents induced in the human body appear as loops inside the human body [52]. Typical sources that generate this type of field are: transformers, inductors, etc.

2. Exposure to high voltage and low current: in this case the dominant field is the electric field. If we consider a point charge, it decreases with distance according to the $1/r^2$ [51]. External electric fields induce a surface charge on the body, resulting in an induced current; the distribution varies depending on the shape and size of the body. Examples of this type of exposure can be found in high power lines, high-power equipment, etc.

In both cases, the induced current depends on the electric field intensity. Usually when this current is relatively high, the human can get simulated in nerve tissues [11]. Our experiment can be considered within the case 2, i.e. an exposure to high voltage and low current, so that the field that is dominant is the electric field.

The demonstrations previously developed allow us to define the equations to be used in our calculation, if we consider the case of time-harmonic exposures at extremely low frequencies [16], the equations obtained by applying the quasi-static approach are:

$$\mathbf{E} = -\boldsymbol{\nabla}V,$$

$$(4.23)$$

$$\mathbf{J} = (\sigma + j\omega\epsilon)\mathbf{E},$$

$$(4.24)$$

$$\boldsymbol{\nabla} \cdot \mathbf{J} = 0,$$

$$(4.25)$$

where $\omega = 2\pi f$ is the operating frequency.

5. RESEARCH METHODS AND MATERIALS

To test the immunity of the implantable cardioverter defibrillator against the ELF electric fields, experiments were conducted in the climate room of the high voltage laboratory at the Tampere University of Technology (TUT). The department EPR Environmental Health had carried out studies on the immunity of the ICD in similar experiments, e.g. under high voltage lines [9] and substations [53], but not within the high voltage laboratory.

As it was a new experiment, a general protocol was analyzed and designed that covered from prior preparation to the conducting of the experiment at the laboratory.

5.1. Experiment

5.1.1. Physical model

As in previous experiments, we use the phantom to house the ICD, because its anatomical shape is very similar to the human body, see Figure 5.1. Different views of the phantom.. This physical model was built from a commercial one (The Rose Spa, Milan Italy) and it was reinforced with silicone to withstand the weight of the liquid and therefore avoid any water leaks. Furthermore, in the design of the phantom all metal was removed, except for a small metal bar that secures the right foot to the wooden board [9]. This model consists of 4-point grounding, 2 hands and two feet, which in turn can be opened for easy dispensing of the water, as show in the Figure 5.1. Additionally, in the left leg was installed a hose to make this process faster.

A coaxial cable, which is immune to electromagnetic interference, was used to connect the ICD inside the phantom. Also the location, where we placed the pacemaker or ICD in our case, corresponds to the position in a human being with similar physical characteristics.

To complete the physical modeling and give more realism, phantom was completely filled with saline solution 0.9 g/L [9], which generates conductivity of approximately $\sigma = 2$ mS/cm, simulating the conductivity inside the human body.
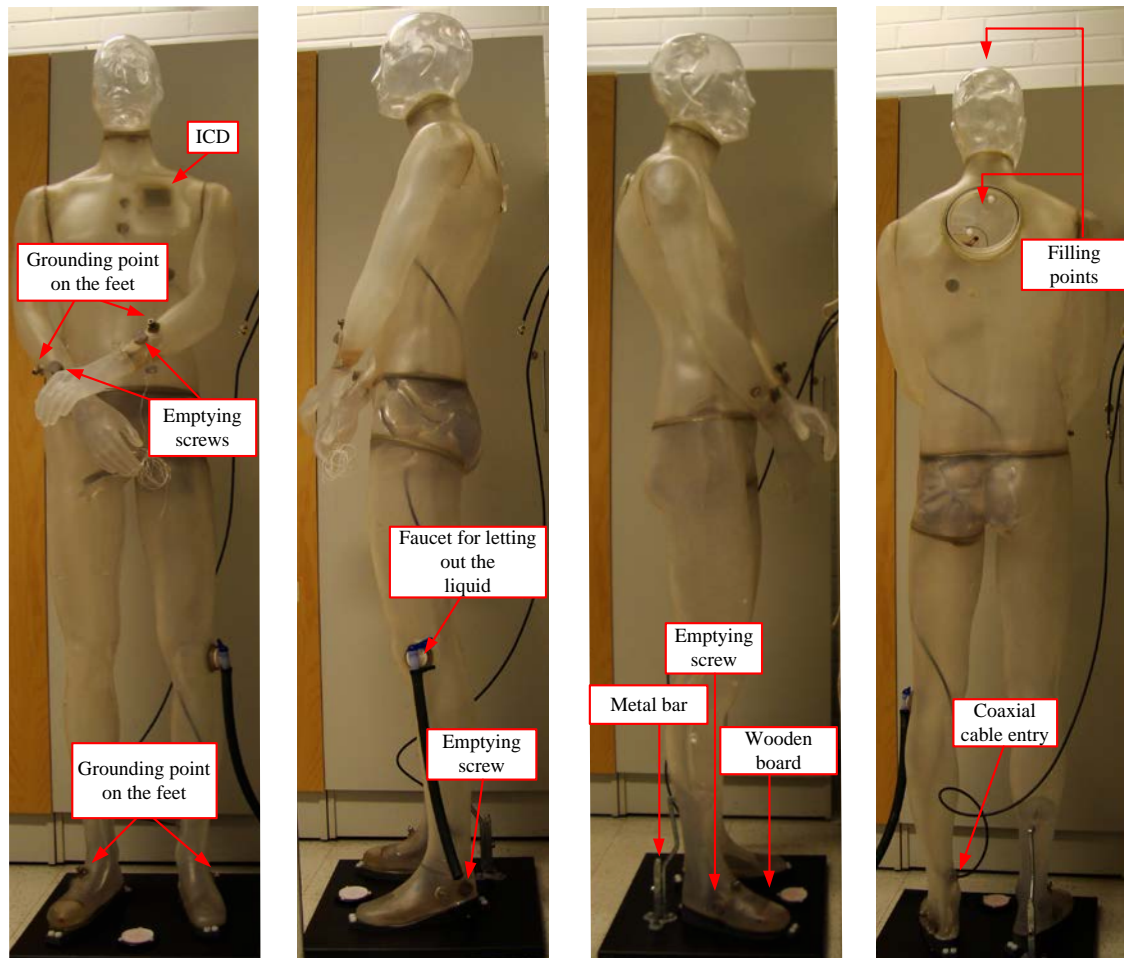
Figure 5.1. *Different views of the phantom.*

5.1.2. Preparation before experiment

Prior to experiment, we check the battery level of the ICD and restart in order to wipe out the counter logs of previous arrhythmias. Simultaneously, we filled the phantom with water and leave it to rest for 4 hours in case if any leaks appeared, and if found to fix them on time. We also prepared the saline solution and made sure we had all the necessary components to carry out successfully the experiment. The day before to the performance, we transported most of these components to make the most of the laboratory hours booked in the hospital.

In order to facilitate the preparation of further experiments, the components used are summarized at the table 5.1.

Table 5.1 *List of components needed to carry out the experiment.*

Components	Comments
ICD + leads	ICD is the component to be tested. It is necessary to reset and check that the battery level is correct.
Phantom and Stand	It is one of the basic components in the experiment. It Must have been previously proven waterproofing.
The laptop computer	It serves as a graphical interface to the oscilloscope. Before going to the laboratory must verify their proper functioning as well as containing the pacing signal
Handy scope HS3	It is used to inject the signal to the ICD
EFA-300 + tripod	Electric field meter
Guidant zoom latitude (PRM)	Used to communicate with the ICD.
Hexagon 520	Multimeter. It is used to measure the induced current in the interior of the phantom.
Dist. 4 WP	Conductivity meter
Thermometer	It is used to measure the water temperature
Groundings cables	It is used to connect the phantom to the ground.
Stools	It facilitates the filling of the phantom.
Tool pack	It consists of items needed, such as rules and meters for measurement.
Drying sheets	There should be no leakage, but if there were they would need to be dried for reasons of electrical safety.
Log book sheets	Enables you to record all data
Water canisters	Contains the saline solution.

5.1.3. Preparation prior to measurement in the laboratory

5.1.3.1 Safety issues and verification of electrode configuration

Before performing any experiment in a climate room it is necessary to check that the bar is connected to ground. This security measure is important.

The first step conducted in the experiment was to verify that the electrode configuration was proven correct. We set the tripod, with the electric field meter, in the central area of the electrodes, with its center at a height approximately 1700 mm above the ground, see Figure 5.2.

Knowing that the distance between electrodes was 750 mm, we could corroborate the value obtained experimentally with the theoretical estimate resulted by applying the equation (4.22).
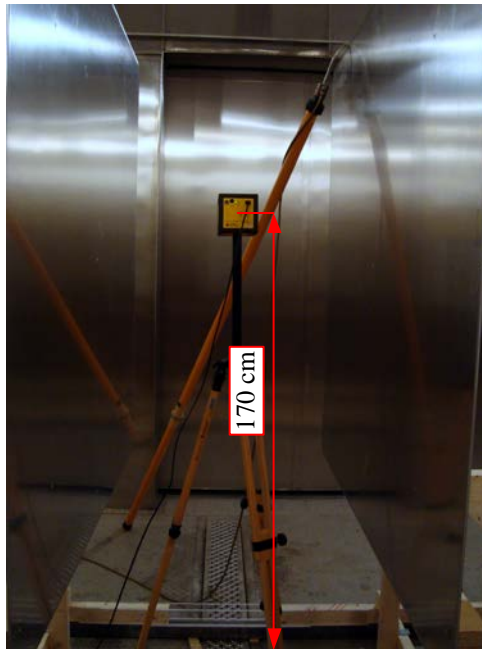
Figure 5.2. Electric field Meter within the parallel plates.

5.1.3.2 Connecting the ICD, positioning, and filling the phantom

Before filling the phantom with saline solution, we have to connect the leads to the ICD and fit them properly with the screwdriver provided by the manufacturer. When we have made the connection, we put the ICD in the correct position and secure it properly so it does not move when the phantom is filled, see Figure 5.3.
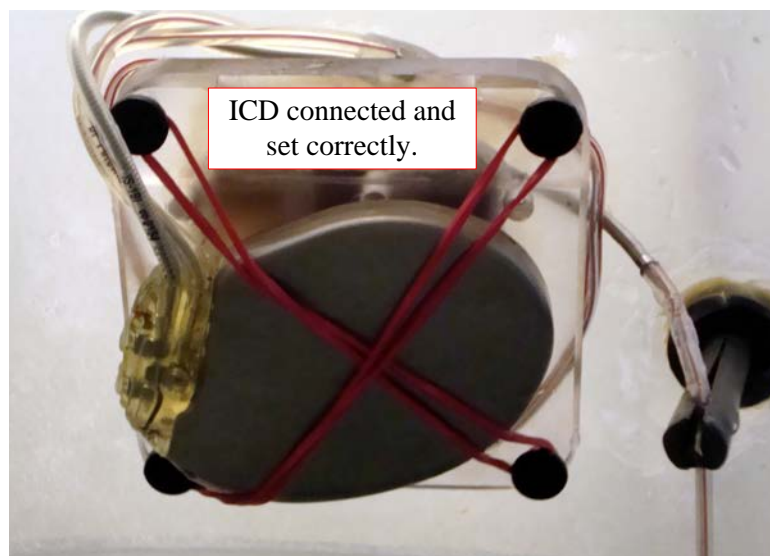
Figure 5.3. ICD properly connected inside the phantom.

When the ICD is placed correctly, Phantom is situated in the desired position. Configurations or settings where measurements were carried out are shown in the Figure 5.4.

Next we insert the water stored in the canister through the orifice in the back and until it is filled up to the height of the ICD and then finish filling through the head. The inner holes (upper extremities, neck 0.04 m 0.035 m, 0.045 m, waist and top of head 0.04 m) allow fluid to flow freely. At this point it may be necessary to make small movements on the phantom, to be performed with caution to avoid losing their water-proofing.

a)   b)
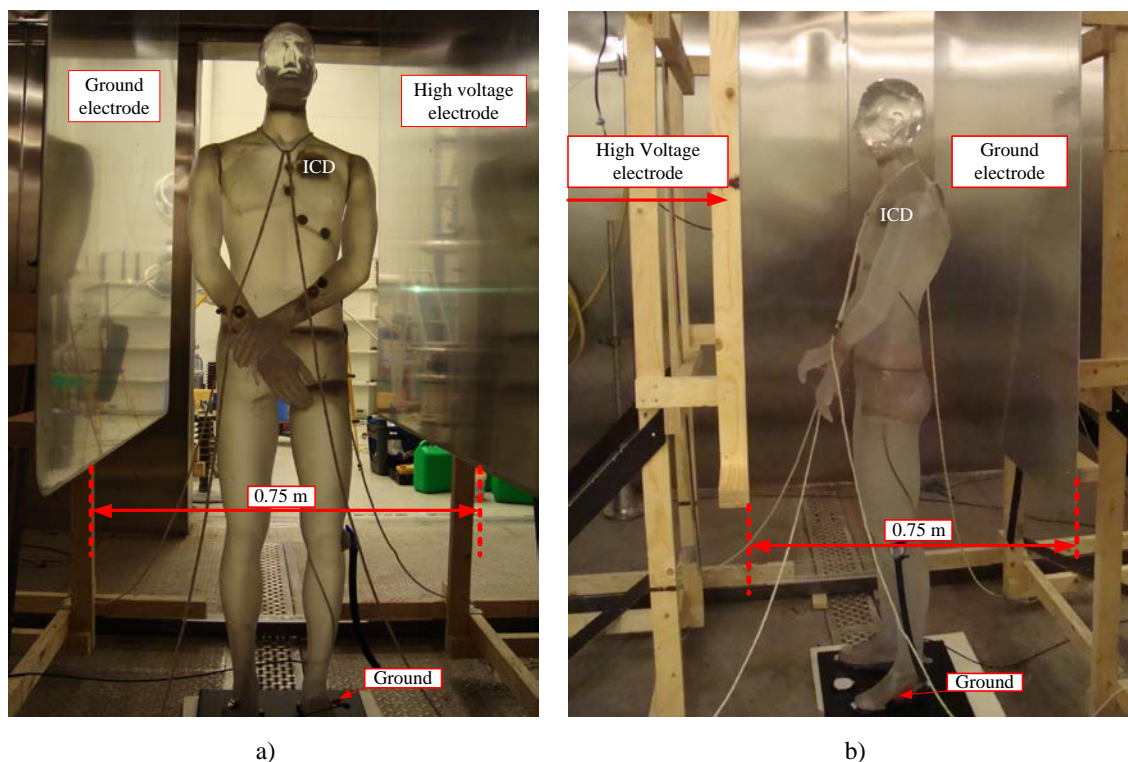
Figure 5.4. Different configurations of the phantom in experiments.

5.1.3.3   Connections and inspections before the start of experiment

Once we complete the previous steps, we proceed to connect the multimeter. This connection allows us to measure the total induced current flowing inside the phantom. The connection to implement is a serial connection, wherein, the meter is located at the end of the grounding. Figure 5.5 a) we can observe the connections to one of the configurations, where the numbers represent the connection points, whereas in Figure 5.5 b) shows how to connect the meter.

The connection of the meter is the last step to perform before the measurement in room, so we must remove the grounding bar and place a safety cone, from this point we cannot enter the room until the end of the measurement.

a)   b)
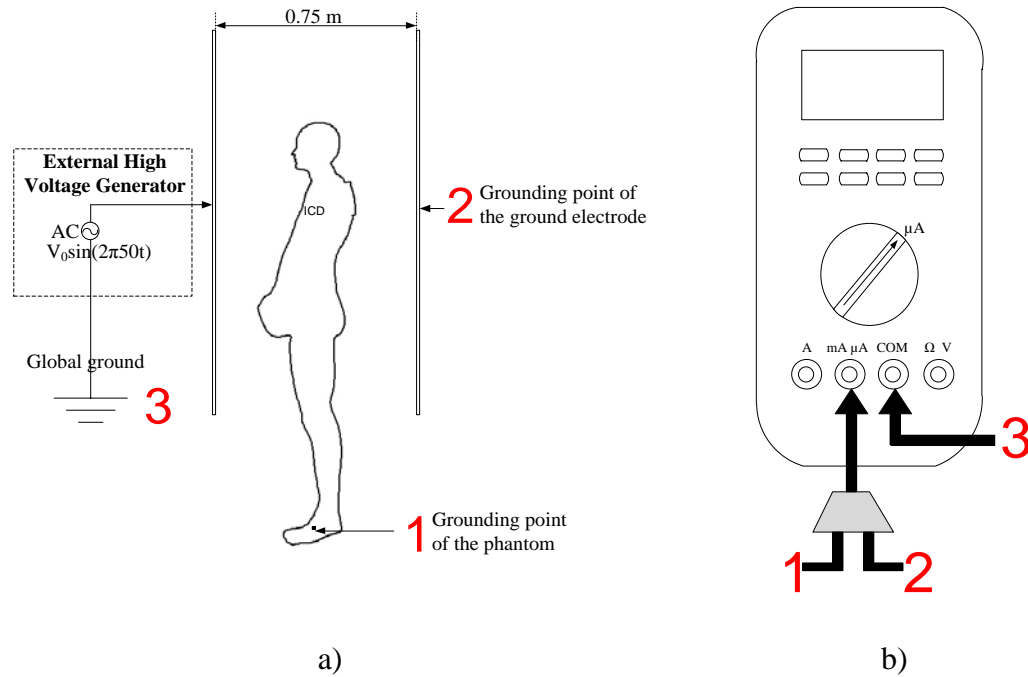
Figure 5.5. *A sketch of the output and input connections from the phantom configuration to the multimeter.*

The signal generator must be connected to the laptop, in order to simulate the heart signal, but the charger must be disconnected because the leakage currents of the laptop could interfere with the measure. To generate the cardiac signal it has been used the same file as in previous experiments, named "kamio_1khz_512.wav" and its waveform is shown in Figure 5.6.
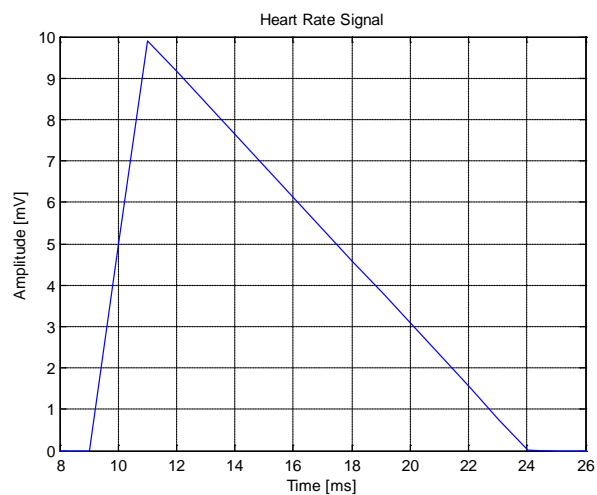
Figure 5.6 *Signal used to emulate the heart rate. Being a wma file, it has to have to use Matlab 2011 b[1] to draw your waveform.*

---

[1] MATLAB is a programming environment for algorithm development, data analysis, visualization, and numerical computation.

Previous checks are completed and we are ready to start the measurement, we inform the lab technician to apply the desired tension and note down in the fact sheet the parameters for the weather in the room (temperature, humidity, etc.). At a safe distance, always behind the safety cone, we see the current values measured by the meter and write down the maximum and minimum, in order to process the data later.

a)   b)
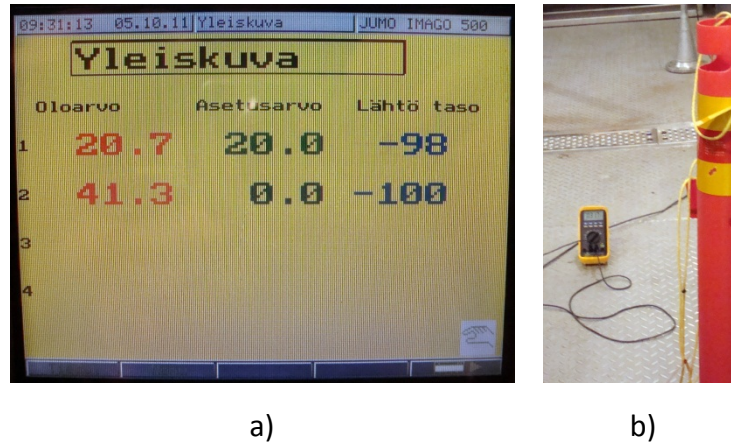
Figure 5.7. a) Reading the moisture and temperature of the room b) Obtaining the total current values from the multimeter. The observer must always behind the cone for safety.

The taking of such action lasted about 5 min, after we checked several parameters to ensure that the experiment was successful. These parameters are: conductivity and water temperature inside the phantom, which should not change if a change is detected, review the configuration because it means that there is an error in one of the points.

a)   b)
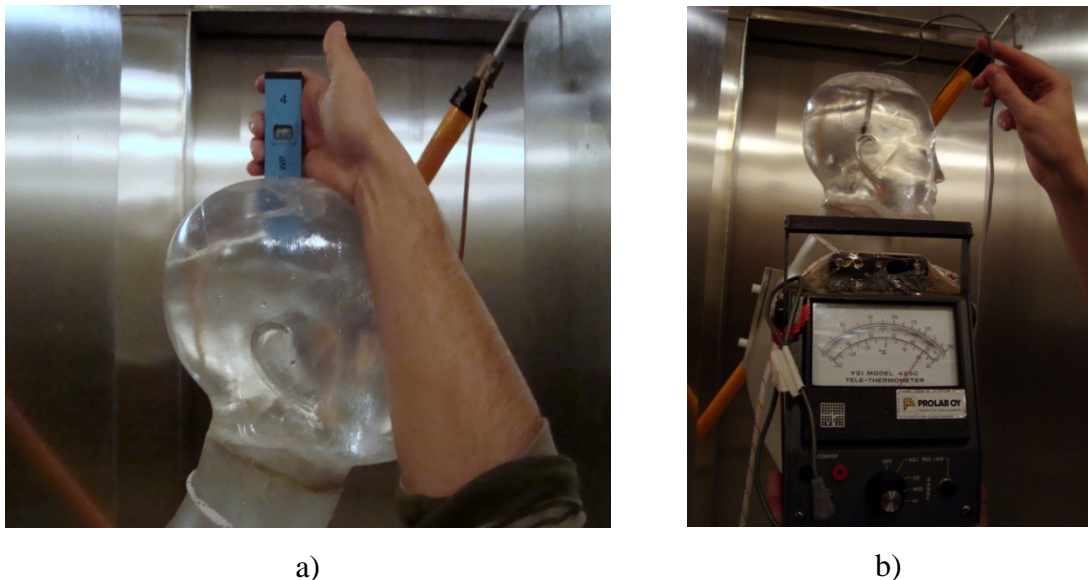
Figure 5.8. The figure a) represent the measuring the electrical conductivity and b) represent a measuring water temperature.

When finished checking the above parameters, we must confirm whether the ICD has received any interference. This is verified by the PRM, which allows us to know if it happened or not any disturbance in the defibrillator, see Figure 5.9.
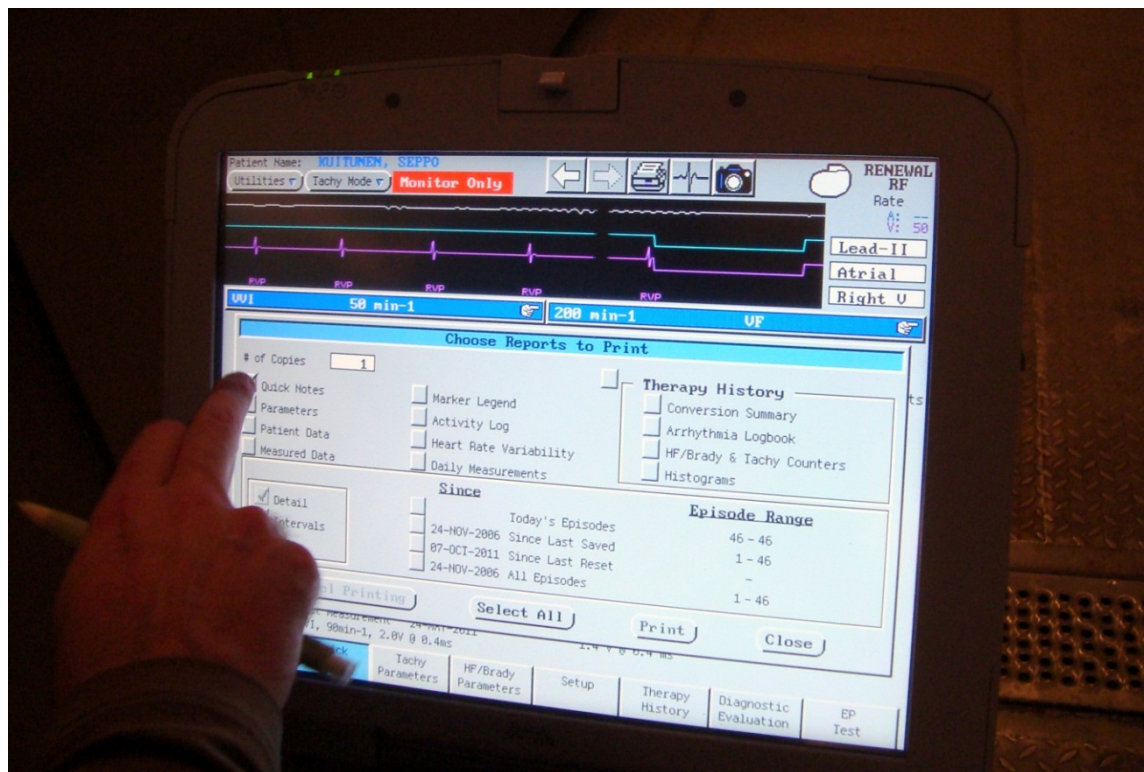
Figure 5.9. *Reading the ICD with the PRM.*

From the experiments it was created a flow chart that summarized algorithmically how the measures carried out, from start to finish as shown in the Figure 5.10.
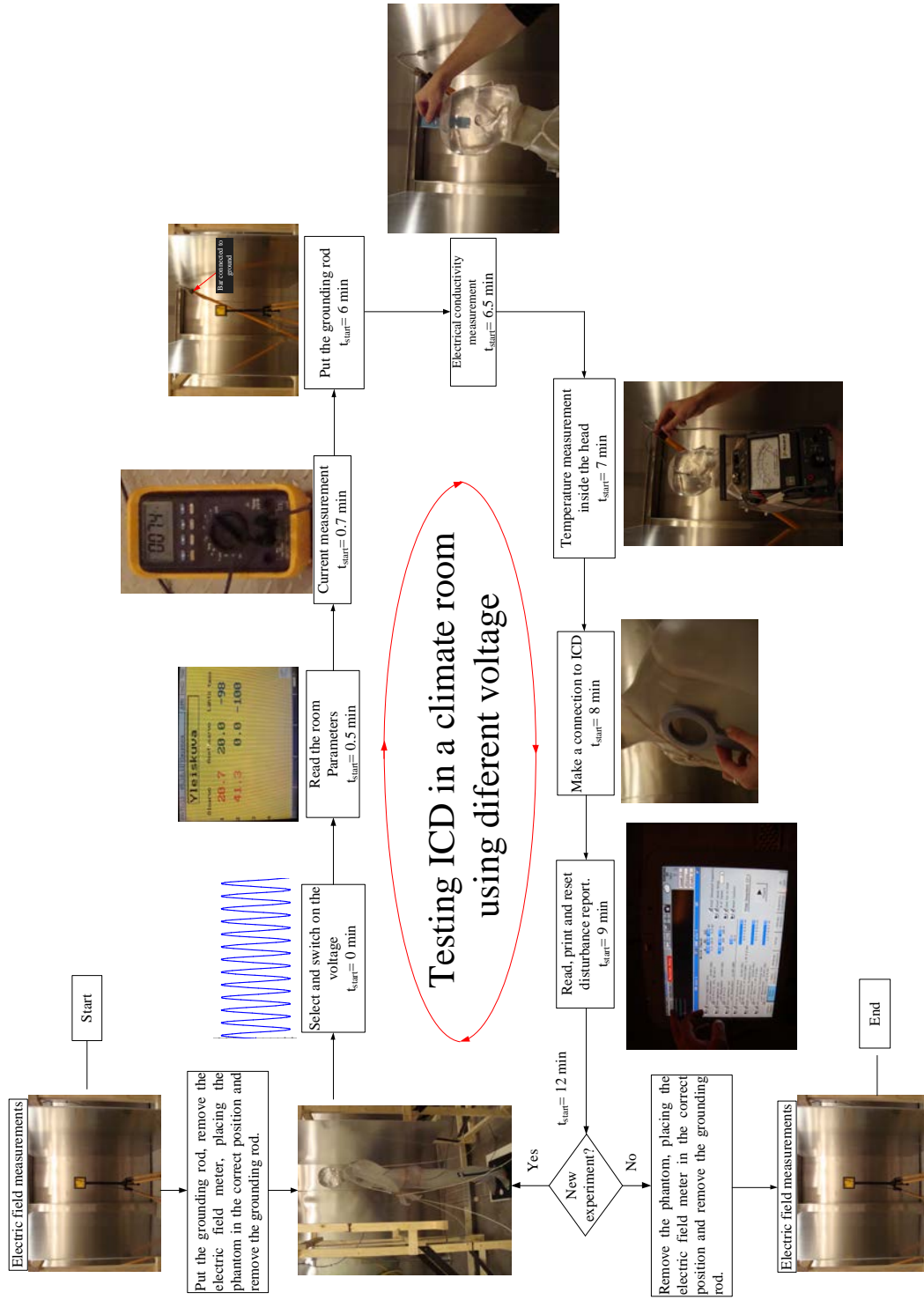
Figure 5.10. Flowchart of the experiment.

5.2.   Calculations performed to corroborate the experiment

The calculations are based on the experiment described previously. Days prior to the experiment, we interviewed the staff of high voltage laboratory, for the purpose of ascertaining the measures and materials of the components that would be used in the experiment.

Using the data provided by the lab master, we created the first model of the phantom. This corresponded to a spheroid, which had the following dimensions: a-semiaxis =1.92/2 m, b-semiaxis = 0.48/2 m, c-semiaxis = 0.48/2 m, corresponding to the same height as the phantom (1.92m) and the same width (0.48m) in front view (the worst case), this model will be defined hereafter as "spheroid model".

This allowed us to get a first approximation of the values of current and electric fields during the experiment.

a)   b)
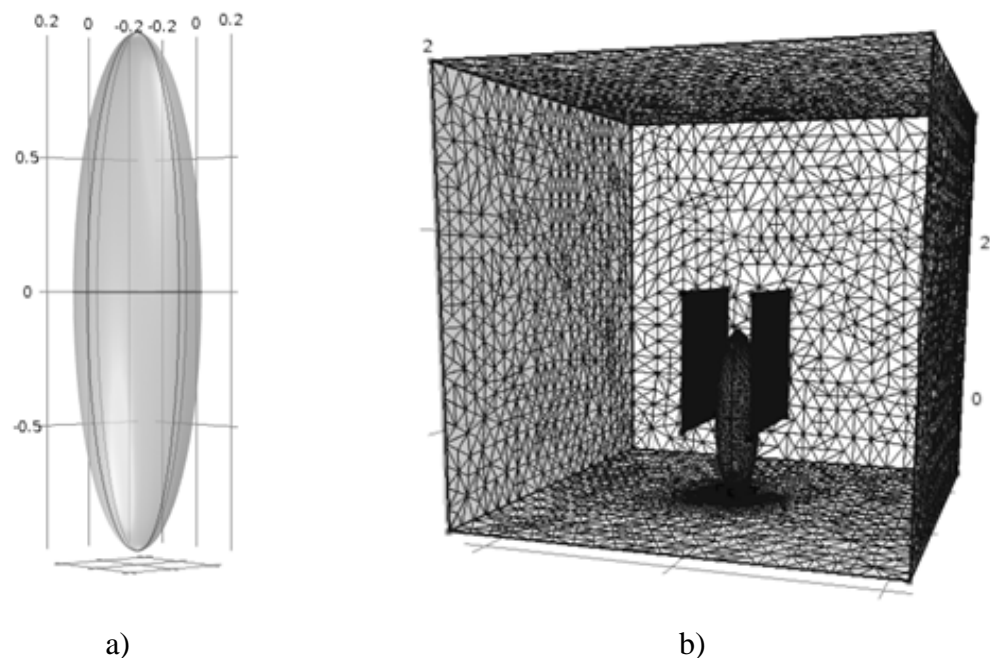
Figure 5.11. *a) Represents the model used, spheroid, while in b) represents the total simulated domain.*

To perform the calculations we used Comsol Multiphysics software. It employs this technique to find the solution to the boundary value problem inserted. The steps to create the model and calculations are explained in the next section.

5.2.1. Finite element methods (FEM)

The Finite element method is a widely used technique for solving numerical multiphysics problems [54]. The methods are used extensively because engineers and scientists can mathematically model and numerically solve very complex problems [55]. FEM allows you to find the solution of boundary value problems governed by ordinary differential or partial equations. FEM creates a finite dimensional approximation of the infinite dimensional boundary value problem.
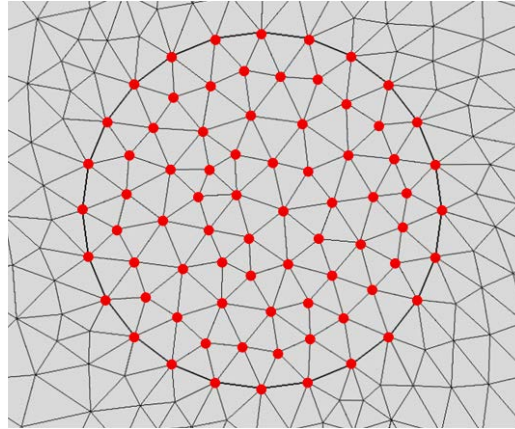
Figure 5.12. This example is a wire through which current flows. The red dots represent the nodes, where will the equations that governing the phenomenon will be solved.

One advantage of this method is its ease of implementation in a computer program, which in turn is a basic condition for use, for the treatment of a particular problem should be a very large number of operations that are performed a practical, fast and accurate at the computer.

There are other known methods for calculating multiphysics problems, such as the finite difference method. In this method the mesh is implemented by rows and columns of orthogonal lines, in FEM each subdivision is unique and need not be orthogonal, for example in 2 dimensions can be triangles and quadrilaterals while 3D are used hexahedral and tetrahedrons.

This thesis is not to make an assessment of which of the two methods is better, since there is a long list of investigations, and each of the methods have their pros and cons. The decision to use FEM was conditioned because the TUT has a campus license to use Comsol Multiphysics and its use did not represent an added cost to the project.

5.2.2. Recreation 3D scene of the experiment

As reflected in the results for the spheroid model, see table 6.1 (page 52) as a first approximation is fine but do not get a very accurate result, since the shape is very different from the real phantom, plus the area affected by the electric field is increased, affecting greater induced current as discussed in the next chapter.

Among the objects that were to be created within the setting of the experiment, the phantom model is undoubtedly the most difficult to create. The model should be such that it is easily importable to the simulation program and also present a very similar way to the physical model.

To make a model as realistic as possible several photographs of the dummy were taken and among them were chosen those that provided more information about the shape of the phantom. After selecting the photo, we imported it into SolidWorks[1], we scaled the image for it to have the original dimensions of the phantom height and corresponding width (192 cm and 48 cm respectively) and by the polyline tool we draw the silhouette of the model, Figure 5.13.

Figure 5.13. Importing into SolidWorks of the model image that was to be created.

When the polyline was completed; we used the extrude tool to create a block that had the front view similar to the polyline, different views can be seen in Figure 5.14.

---

[1] SolidWorks is a 3D mechanical CAD (computer-aided design) program that runs on Microsoft Windows and is being developed by Dassault Systèmes SolidWorks Corp.
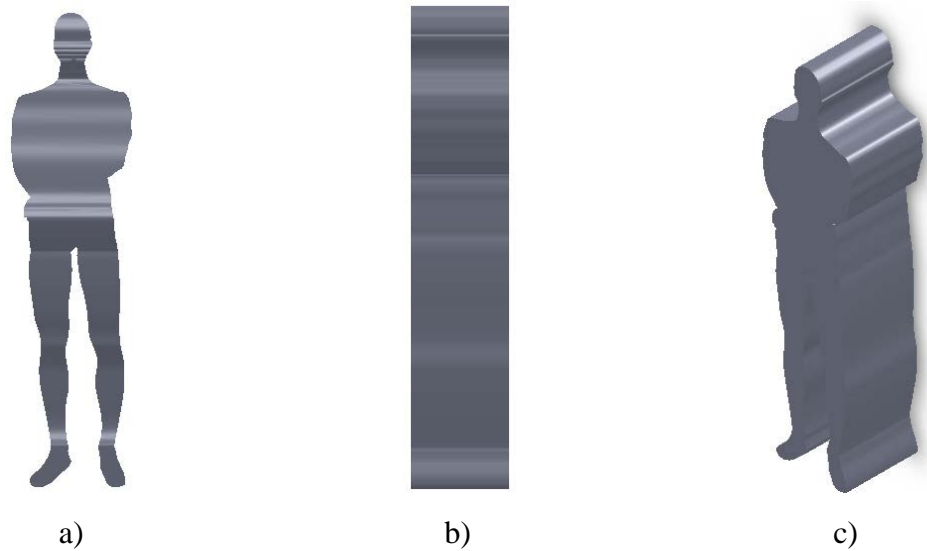
Figure 5.14. *a) front view, b) Side view, c) isometric view of the phantom model, at an intermediate point of the creation process.*

The model we got here it is more accurate than the spheroid model but it is not as precise as we would want it to be. Although frontally is similar to the real model, laterally is completely different. Using the same technique described above it was performed two lateral cuts. The Figure 5.15 shows the polylines made to carry out the cuts.

The first of the cuts, light blue, resulting in the model shown in Figure 5.15.
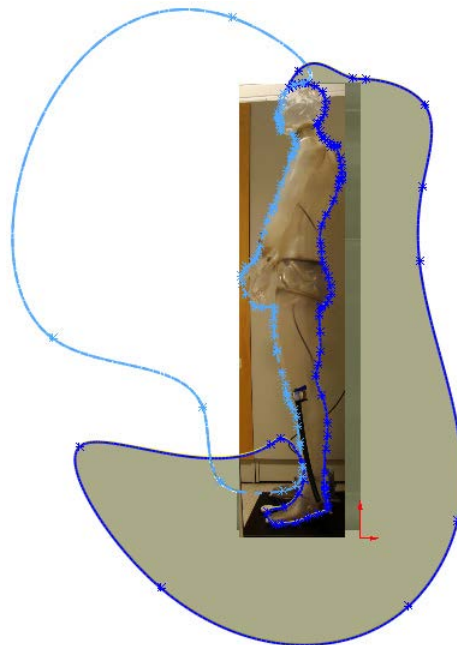
Figure 5.15. *Polylines created to make lateral cuts*

The view after the first cut is shown in the Figure 5.16.

Figure 5.16. *a) front view, b) side view, c) isometric view of the phantom model, at an intermediate point of the creation process.*

The second cut, dark blue, allowed us to obtain a very similar model in the end, see Figure 5.17b).

Figure 5.17. *front view, b) side view, c) isometric view of the phantom model in the previous step to the final model.*

The model that we obtained in Figure 5.18 was not ready to be imported into Comsol Multiphysics because the cuts made had created edges with very steep transitions, which usually makes difficult the generation of the mesh. For this reason each edge was smoothed successfully obtaining the mesh, as seen in Figure 5.18. This model will be defined as a phantom model.
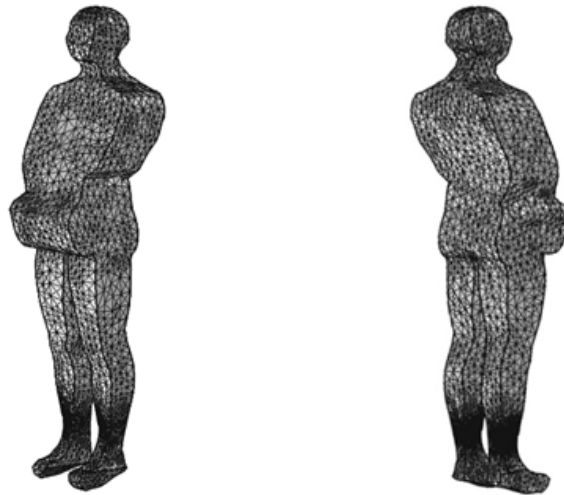
Figure 5.18. *Different view of the mesh created in Comsol Multiphysics.*

To complete the design of the two scenarios we created the electrodes, based on the specifications of the laboratory teacher. Based on these data, the electrodes were made of aluminum and were separated by a distance of 750 mm, had a size of (width 1500mm, height 1500mm and thickness 3mm) in addition, to decrease the ends effect it has been applied a fillet radius of 15 mm in each of the corners of the electrodes. The result of adding the electrodes to the model is shown in the Figure 5.19.
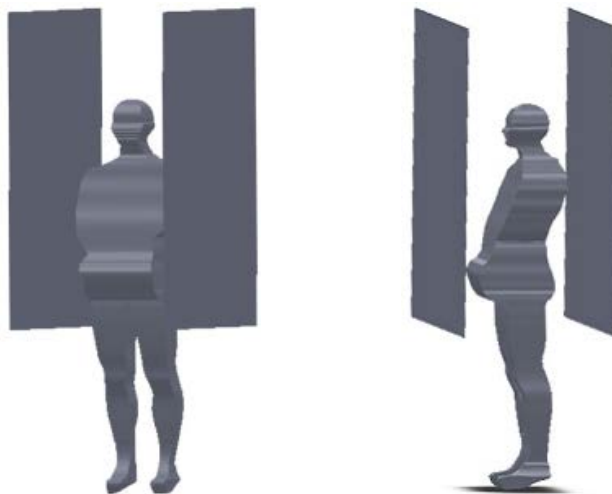
Figure 5.19. *Different positions of the phantom within the parallel plates, as performed in the experiments.*

To complete our domain we lack only the walls of the laboratory, and because they are grounded, they intervene in the calculation. Therefore they will be created in Comsol Multiphysics, to facilitate the construction.

5.2.3. Importing the Comsol Multiphysics model, mesh generation and definition of the materials

Once we have created most of the domain to simulate what Comsol Multiphysics to import. This import is done using the module 3D CAD import of this software. As mentioned earlier, we needed to build the walls of the laboratory, which we were created using a cube in both scenarios.

When it was found that the mesh was correct, it was assigned to each element its corresponding material. All materials were obtained from the material library of Multiphysics Comsol 4.2a, the allocation made can be seen in Figure 5.20.
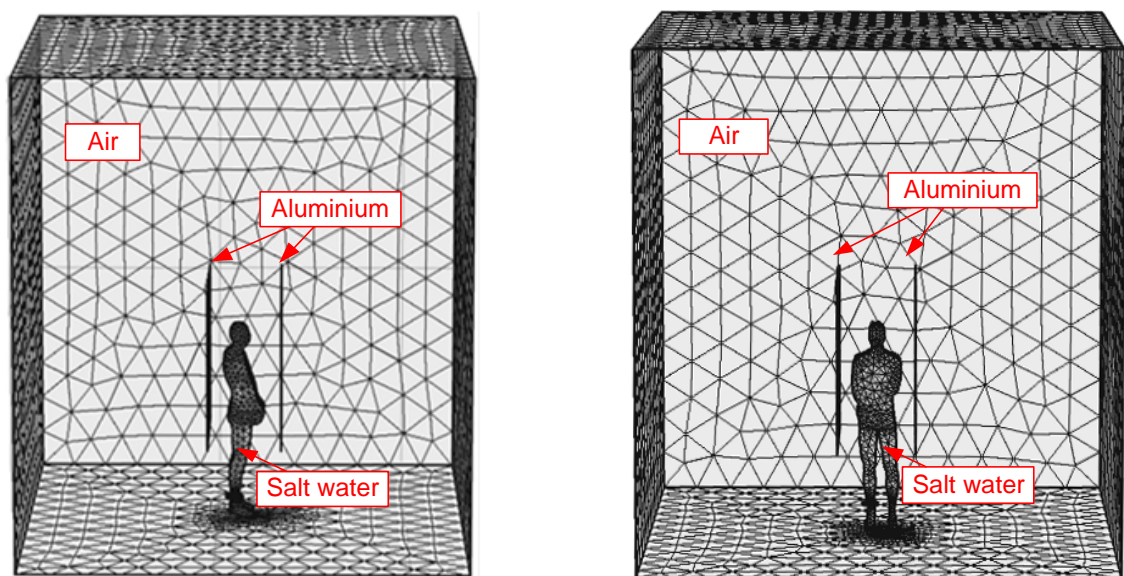
Figure 5.20. Generation of the mesh to simulate the different domains within Comsol Multiphysics.

To calculate the total induced current we had to integrate the current density on a surface. The area chosen was the phantom's left foot because it was grounded. In order to avoid a discontinuity in the domain to simulate, the center of the disc intersected with the phantom model was assigned salt water as material, while the outside was assigned air, creating continuity, see Figure 5.21.
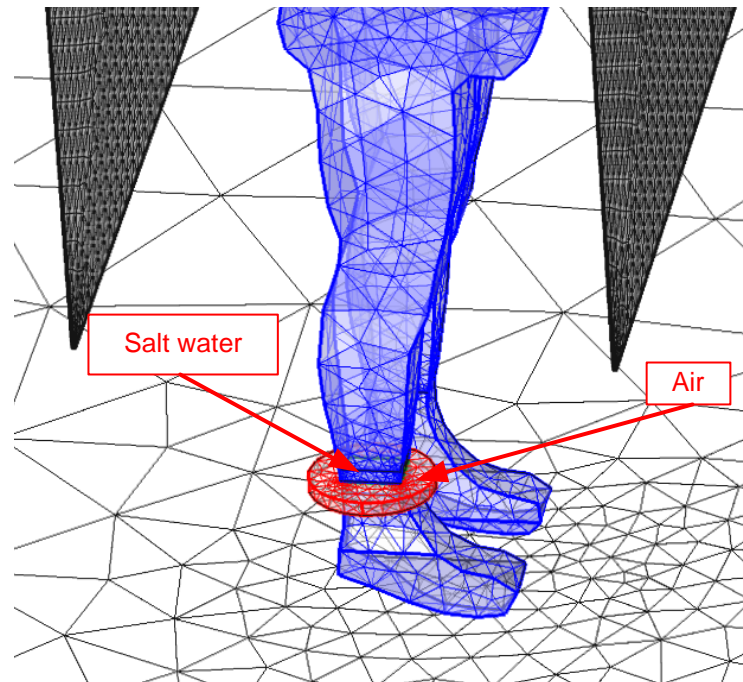
Figure 5.21. *Representation of the disc in the left foot that will allow us to integrate the current density on the surface. Also shows the assignment of materials in said foot.*

5.2.4. Governing equations and boundary conditions

The quantities that we wanted to calculate in our simulation domain were the electric field and the induced current inside the phantom model, for this, starting from Maxwell's equations and Constitutive Relations, and also imposing the condition of quasi-static; we concluded that the equations used are.

$$\nabla \cdot \mathbf{J} = 0,$$

$$\mathbf{J} = (\sigma + j\omega\epsilon_0\epsilon_r)\mathbf{E},$$

$$\mathbf{E} = -\nabla V.$$

These equations are included within the module electric current of Comsol Multiphysics 4.2a. To solve these equations it was imposed the boundary conditions. As can be seen in Figure 5.22, it has been imposed that in the domain walls, the left foot and one of the plates (blue), the potential was $V = 0$; while the other plate (red) is where the high voltage generator is connected with signal amplitude V_0, and frequency f=50 Hz.
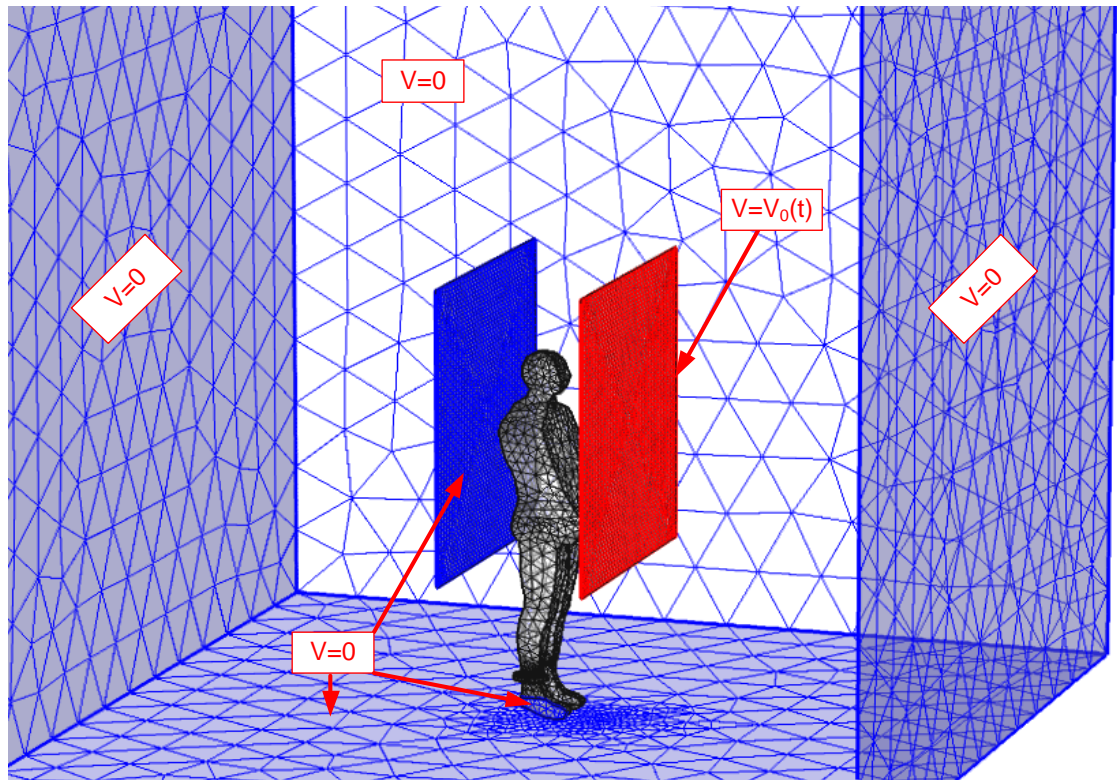
Figure 5.22. Representation of the boundary conditions.

Once the boundary conditions imposed we are ready to perform the calculations, the results will be explained in the next chapter.

5.2.5. Calculation validation

To validate the numerical method used, we calculated the model of a prolate spheroid half. This method has been used by other researchers to demonstrate their methods of calculation [57]. The semi-spheroid has the following semi axes a = 1.7m and b = 0.3m, also presented a homogeneous conductivity of 0.1 S/m. An electric field of 1 kV/m was applied externally. In this case, the internal electric field can be calculated analytically by the equation [58].

$$E_i = \frac{E_0}{\left\{1 + \left(\frac{\sigma}{\omega\epsilon_0} - 1\right)(u_0^2 - 1)[u_0\coth^{-1}(u_0) - 1]\right\}} \tag{5.2.1}$$

In the equation (5.2.1) ϵ_0 represent the permittivity of the surrounding medium (air), and u_0 is calculated as follows:

$$u_0 = \left[1 - \left(\frac{b}{a}\right)^2\right]^{-\frac{1}{2}} \tag{5.2.1}$$

The frequency calculation was 50 Hz. The electric field inside the semi-spheroid is calculated analytically 0.593 mV/m while if we calculate numerically obtained is of 0.597 mV/m, the relative error obtained is 0.67%.

On the other hand if we compare analytically and numerically the current value (I[μA]) along the major axis of the spheroid (z[m]); we obtain that, in the worst case, corresponding to the bottom of the spheroid, we get a relative error of 0.96%, see Figure 5.23.
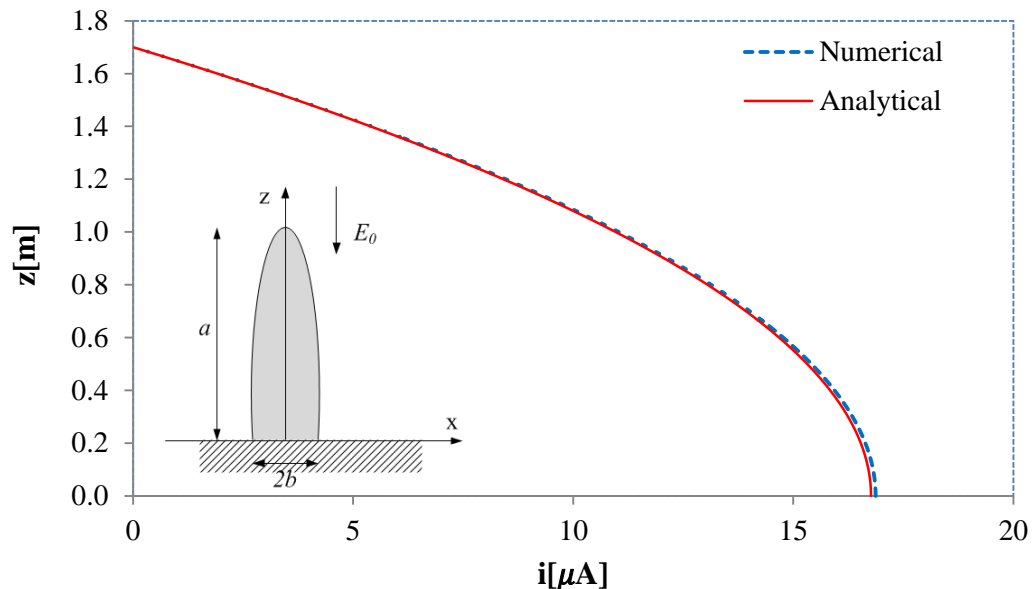
Figure 5.23. *Comparison between the calculated values obtained numerically and analytically.*

6. RESULTS AND DISCUSSIONS

6.1.   Evaluation of the measurement process

The protocol stated that a prior check of the separation between the parallel plates has to be done. Measuring the electric field inside the plates, using the equation set forth above (4.22), the values obtained allow us to determine whether the separation between them is correct. This step was performed each day at the beginning of each experiment.

Comparing the data obtained through the EFA-300 meter and the theoretical value can be seen that maximum relative error is less than 5% and 0.5% on the first day of experiment and second, respectively, see Figure 6.1a) and Figure 6.2a). With this result, we can say that the separation between the two parallel plates in both cases is correct (0.75m).

Additionally, the protocol stated that it has to be check that the conditions in the controlled climate room did not vary significantly. One of the checks was to verify that they had not changed or altered the electrode gap. For this, the electric field was measured at the beginning and end of each day of the experiments see Figure 6.1b) and Figure 6.2b). Those figures show that indeed, there have not been changes in the configuration of the parallel plates, since the maximum relative error is less than 1% and 2.5%, in the first and second day of experiments, respectively.

a)   b)
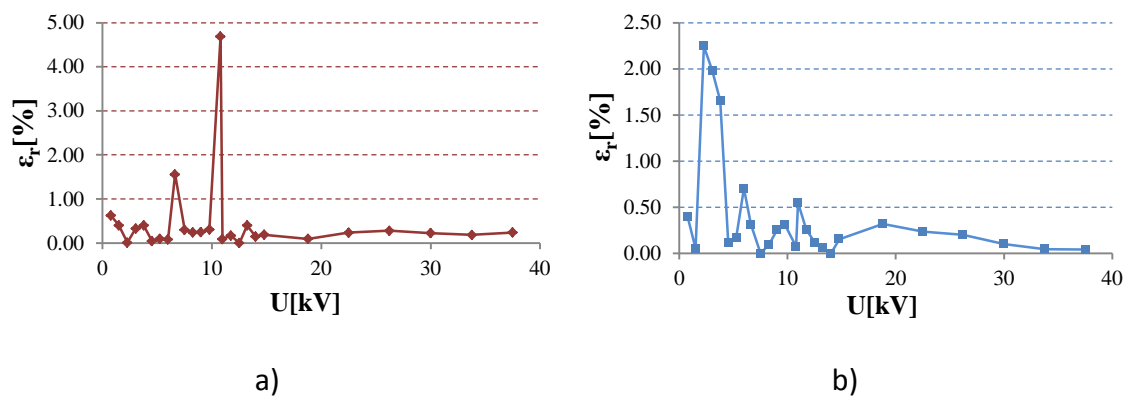
Figure 6.1 *Data from the first day of the experiments. Where a) represents the relative error between the measurements prior to the experiments and the analytical value, whereas in b) it represents the relative error between measurements of the electric field taken prior and after experiments.*

a)   b)
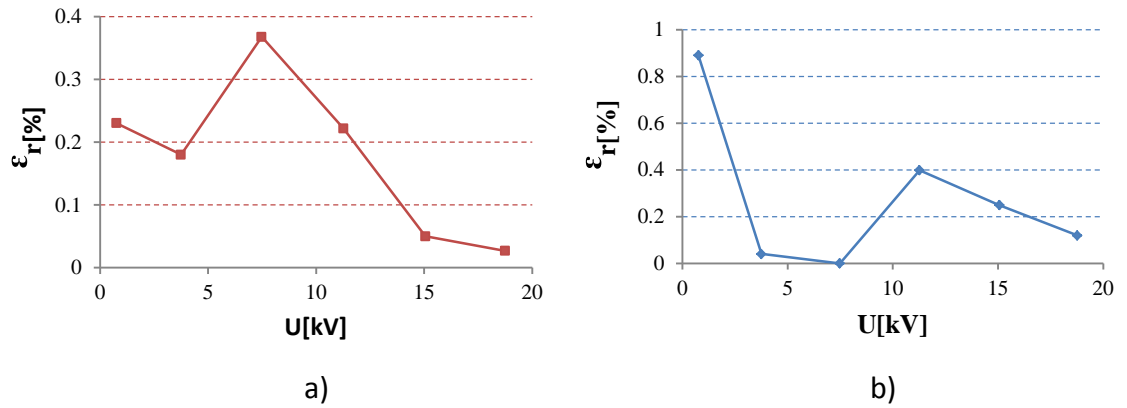
Figure 6.2 Data from the second day of the experiments. Where a) represents the relative error between the measurements prior to the experiments and the analytical value, whereas in b) it represents the relative error between measurements of the electric field taken prior and after experiments.

Others parameters evaluated were the electrical conductivity σ[mS/m] and the temperature inside the phantom. In both days of the experiments, these values did not change significantly. Because we use the same water in both experiments, the conductivity remained two days between $2.02 \leq \sigma \leq 2.2$ [mS/m], see Figure 6.3a) and 41a) reasonable values for the salt concentration inside the water. On the other hand, the temperature also remained relatively stable $20.5 \leq T \leq 23.5$ ºC, see Figure 6.3) and 41b). The small increases observed coincide with the increase in the room temperature.

The shape of the lines between the two days of experiments is different. On the first day the applied voltage, unlike the second day, was not always increasing; which explains why they have test points in both directions, increasing and decreasing.

a)   b)
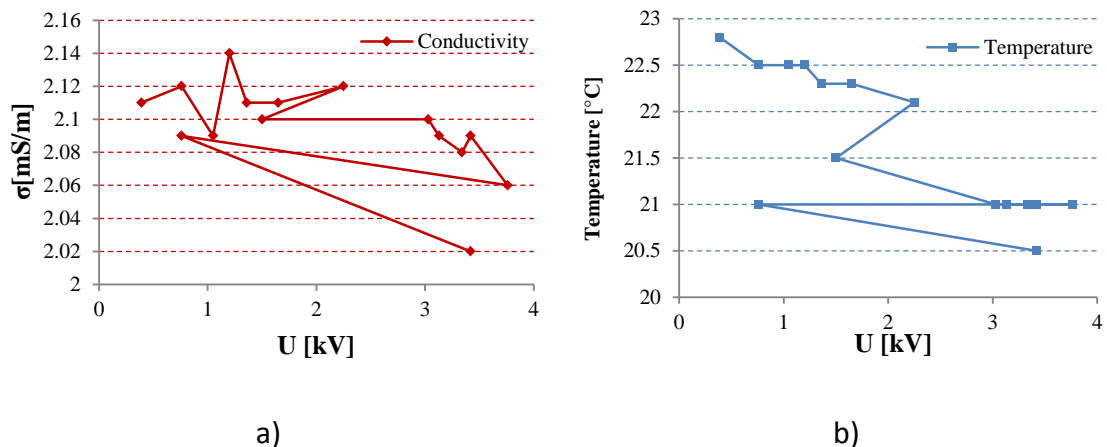
Figure 6.3 Data from the first day of the experiments. Where a) is represented the electrical conductivity in each measurement. Also in b) is represented the temperature in each measurement.
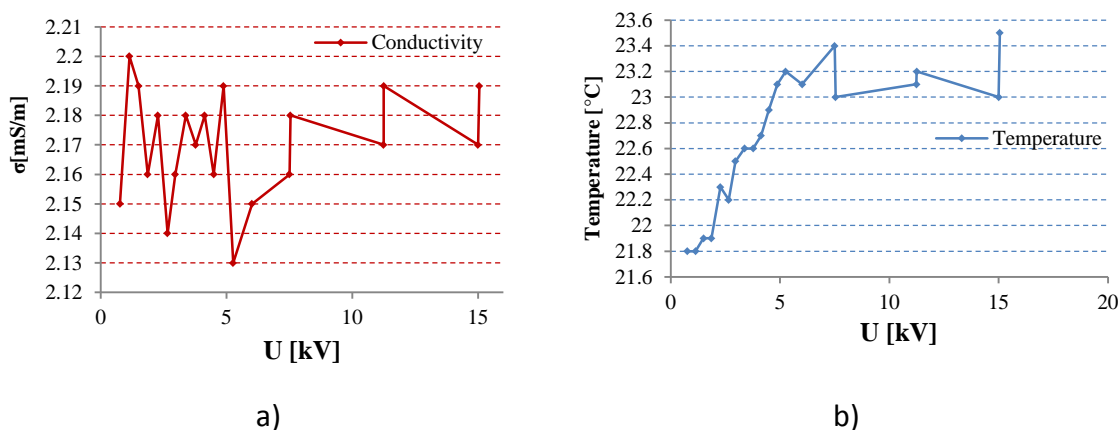
Figure 6.4 *Data from the second day of the experiments. Where a) is represented the electrical conductivity in each measurement. Also in b) is represented the temperature in each measurement.*

6.2.   Reading the implantable cardioverter defibrillator

The first day, the implantable cardioverter defibrillator used was the same throughout the experiment (Guidant Vitality 1870). For each voltage that was applying, the ICD was interrogated using the PRM and the histogram of episodes was printed, then was restarted to apply the next voltage.

For applied voltages between 0.76 kV and 3.76 kV, was obtained in all cases at least, one interference, see appendix II. In contrast, on the second day, the ICD tested was Guidant Renewal 4 RF HE H239 and with voltages ranging from 0.76 kV to 15.4 kV did not get any interference.

With these results it is difficult to obtain a logical pattern of when the interferences appear.

6.3.   Potential and electric field within the parallel plates for both configurations

When between the parallel plates there were only dielectric, the air in our case, the electric field in the central area of the plates was uniform, as discussed in previous chapters.

But when the phantom was placed inside the plates, the electric field was no longer uniform (Figure 6.11, 6.10). If we had inserted the meter EFA-300, the value that would give us will be a local value, i.e., a little displacement of the meter within the parallel plates will give us a quite different value of the electric field.

One advantage of performing the numerical calculation, in our case, using the technique FEM is that we can represent magnitudes that are physically impossible to measure or are very expensive. Some examples are equipotential lines within the plates (Figure 6.5, 6.5, 6.7) and electric field lines (Figure 6.8, 6.9, 6.10).

The following figures represent the equipotential lines in kV, for the spherical model and the phantom model, when was applied a voltage of 15 kV in the positive electrode.
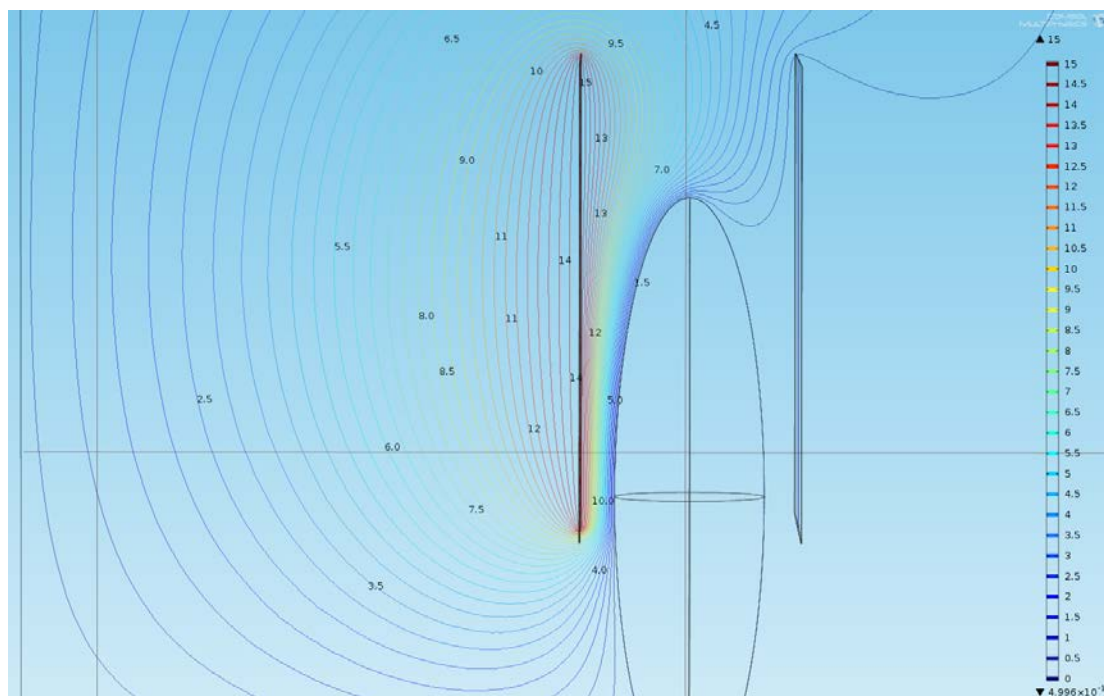
Figure 6.5 *Three-dimensional simulation performed in Comsol Multiphysics of the spherical model, the mesh consisted of 348106 elements. The slice represents the equipotential lines in kV when are applied in the high voltage electrode a voltage of 15 kV.*
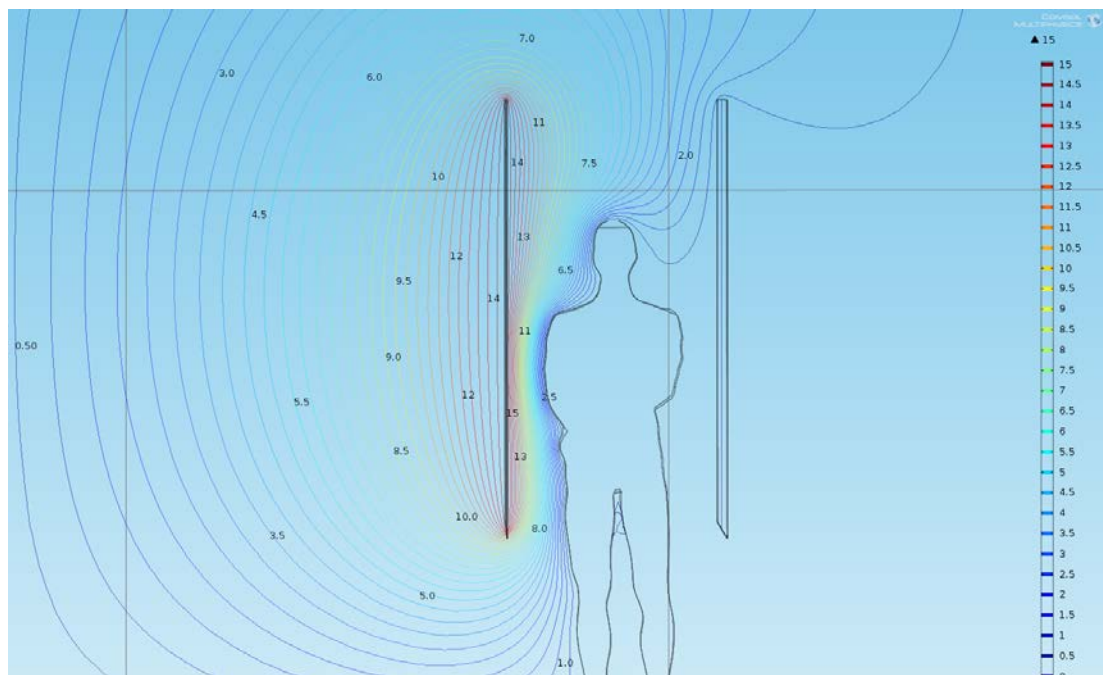
Figure 6.6 *Three-dimensional simulation performed in Comsol Multiphysics of the phantom model, the mesh consisted of 209251 elements. The slice represents the equipotential lines in kV when are applied in the high voltage electrode a voltage of 15 kV. Corresponds to the front configuration.*
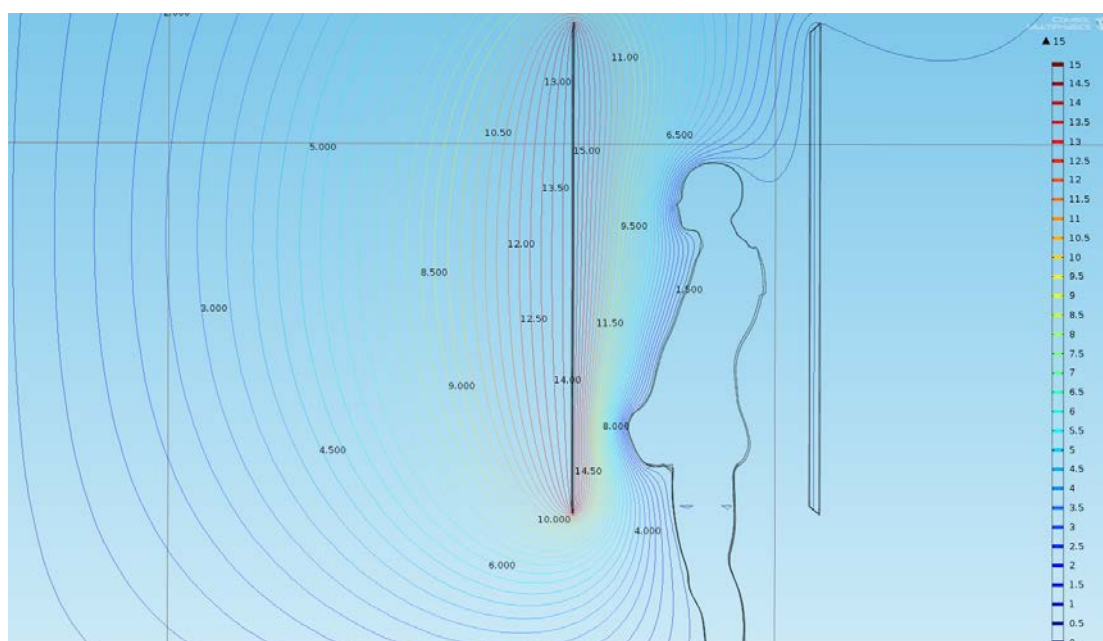
Figure 6.7. *Three-dimensional simulation performed in Comsol Multiphysics of the phantom model, the mesh consisted of 215401 elements. The slice represents the equipotential lines in kV when are applied in the high voltage electrode a voltage of 15 kV. Corresponds to the lateral configuration.*

6.3.1. Contour of electric field magnitude

Analyzing the equipotential lines of the previous figures, we can see that the greatest gradient corresponds to the spherical model. While the smaller gradient corresponds to the lateral configuration of the phantom model. As the electric field is equal to minus the gradient of electric potential, hopefully we get values more intense of the electric field in the spherical model. This result is shown in the following figures:
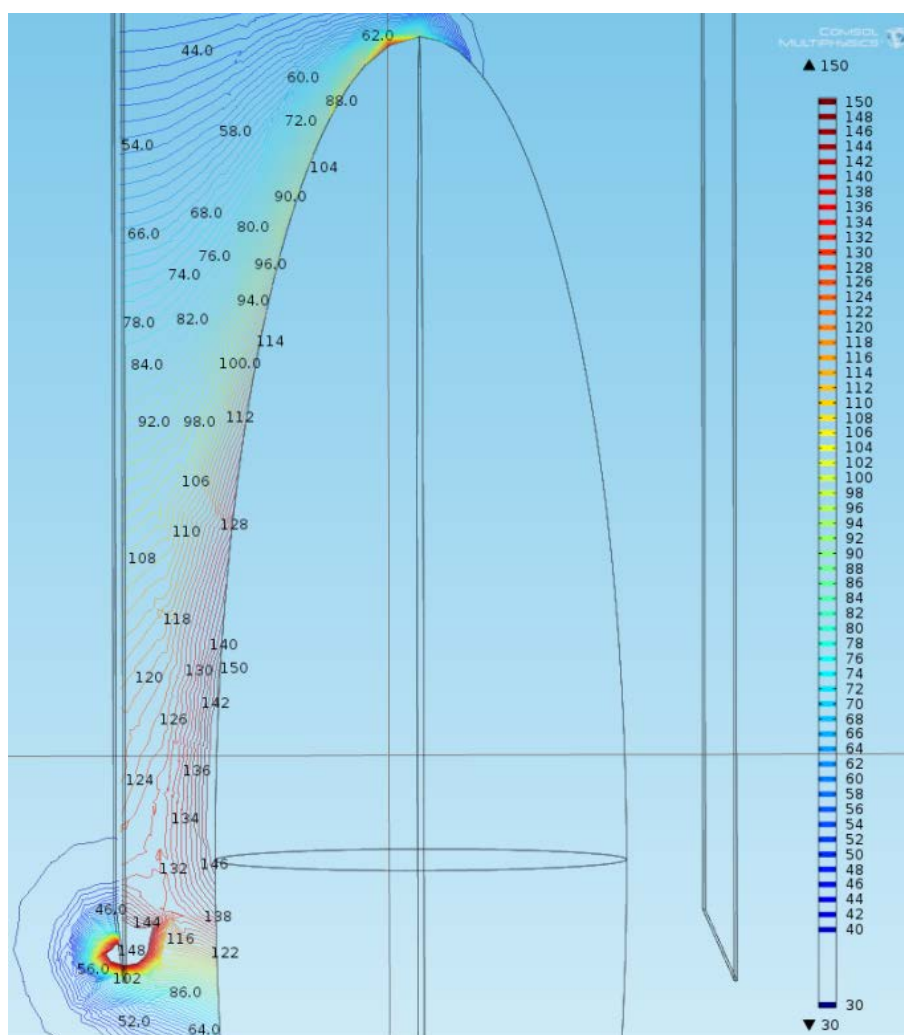
Figure 6.8*. Three-dimensional simulation performed in Comsol Multiphysics of the spherical model. The slice represents the contour lines of the electric field when are applied in the high voltage electrode a voltage of 15 kV.*
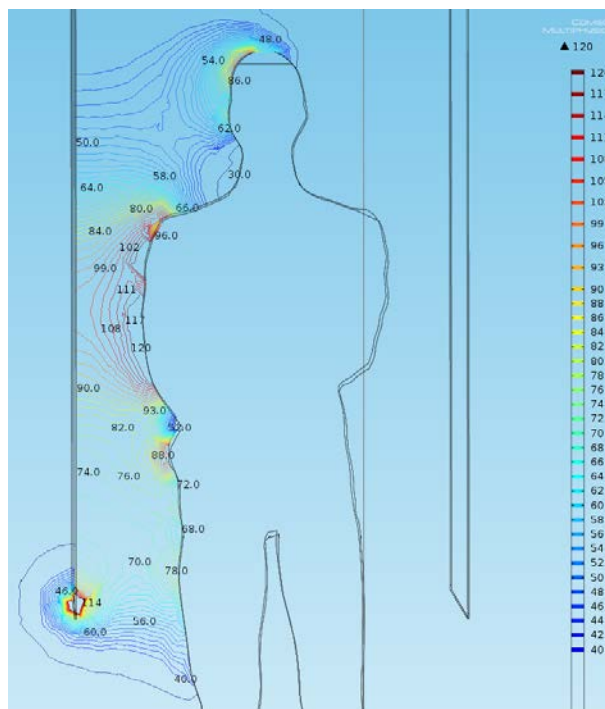
Figure 6.9. Three-dimensional simulation performed in Comsol Multiphysics of the phantom model. The slice represents the contour lines of the electric field when are applied in the high voltage electrode a voltage of 15 kV. Corresponds to the front configuration.
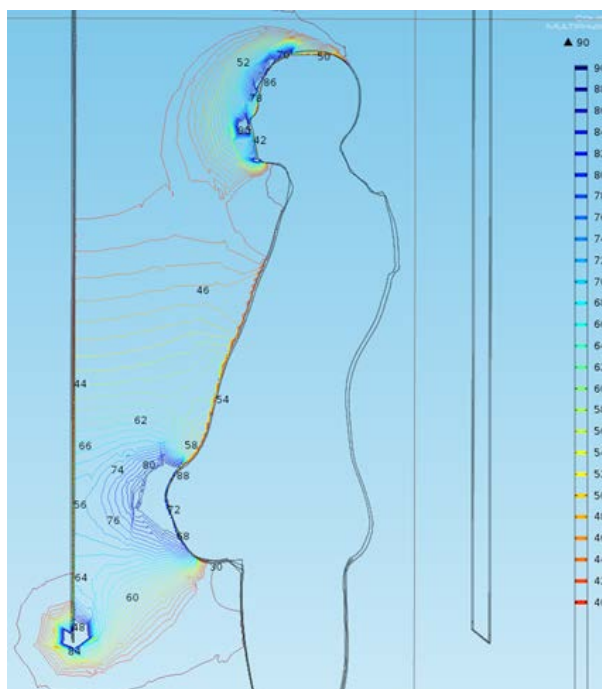
Figure 6.10 Three-dimensional simulation performed in Comsol Multiphysics of the phantom model. The slice represents the contour lines of the electric field when are applied in the high voltage electrode a voltage of 15 kV. Corresponds to the lateral configuration.

6.4. Total induced current within the phantom

Previous simulations show that, the electric field strength is higher in the spherical model, while the lateral configuration of the phantom model has lower electric field strength. This result is in complete agreement with what we expected. This implies that the spherical model has higher current density, which explains that this model has a higher total induced current.

Comparing the different configurations of phantom model, we see the front configuration has a higher the electric field strength, as we explained above, this will make the total induced current in this configuration is higher than the lateral configuration.

However, following the steps in the previous chapter, it was possible to measure the total induced current inside the phantom. On the first day of experiments and in most of the second, the phantom was placed on the inside of the parallel plates according to the lateral configuration. Near the end of the second day, the phantom was turned 90 degrees clockwise and was performed 3 measures in this configuration (front configuration). At the table 6.1 we can see experimental and calculated values for the lateral configuration.

Table 6.1 Values obtained of induced current within the phantom as a function of voltage. The values were also calculated with models, spherical model and phantom model in the lateral configuration, and the relative error in percent.

#	U [kV]	I_{AVG} [μA] Measured	Calculated Phantom	Calculated Spheroid	ϵ_r [%] phantom	ϵ_r [%] Spheroid
1	0.76	7.55	7.53	11.55	0.20	52.96
2	0.76	7.40	7.53	11.55	1.82	56.06
3	0.76	7.25	7.53	11.55	3.93	59.29
4	0.76	8.60	7.53	11.55	12.38	34.28
5	1.05	11.20	10.41	15.96	7.05	42.46
6	1.14	10.95	11.30	17.32	3.22	58.20
7	1.2	12.60	11.90	18.23	5.58	44.72
8	1.36	14.90	13.48	20.67	9.51	38.70
9	1.5	15.80	14.87	22.79	5.88	44.26
10	1.5	14.05	14.87	22.79	5.85	62.23
11	1.65	16.40	16.36	25.08	0.25	52.94
12	1.86	16.50	18.44	28.26	11.76	71.29
13	2.27	20.55	22.51	34.49	9.52	67.85
14	2.65	24.05	26.27	40.27	9.24	67.43
15	2.96	26.05	29.35	44.98	12.65	72.66
16	3.03	29.50	30.04	46.04	1.83	56.07
17	3.13	30.20	31.03	47.56	2.75	57.49
18	3.34	31.80	33.11	50.75	4.13	59.60
19	3.38	29.25	33.51	51.36	14.57	75.59
20	3.42	31.20	33.91	51.97	8.68	66.56
21	3.63	32.20	35.99	55.16	11.77	71.30
22	3.76	32.00	37.28	57.13	16.49	78.55
23	3.77	32.60	37.38	57.29	14.65	75.73
24	4.13	36.15	40.95	62.76	13.27	73.60
25	4.49	38.20	44.52	68.23	16.53	78.60
26	4.88	42.25	48.38	74.15	14.51	75.51
27	5.26	45.75	52.15	79.93	13.99	74.70
28	6.01	51.75	59.59	91.32	15.14	76.47
29	7.5	64.65	74.36	113.97	15.02	76.28
30	11.25	95.45	111.5	170.95	16.85	79.10
31	15.05	134.10	149.2	228.69	11.27	70.54

As we explained earlier, the spheroid model has a very high relative error; on average have a 63.58%. This is because the electric field intensity is higher in this model also be taken into account that the surface is exposed to these fields is greater. This makes this model can only be used to obtain only the order of magnitude of total induced current, but in no case an accurately value.

On the other hand if we analyze the phantom model, the value we get is much more precise, only 9.36% relative error on average. This value is an acceptable value, as we didn't know the exact materials of the physical model. Also in the hands of the phantom model differs from the real model, which makes more surface exposed to the electric field, generating a slight increase in the current value.

If the total induced current is represented as a function of applied voltage, see Figure 6.11, we see that both the numerical values and measured have a proportional relationship between with the applied voltage, which is in total agreement with the theory.
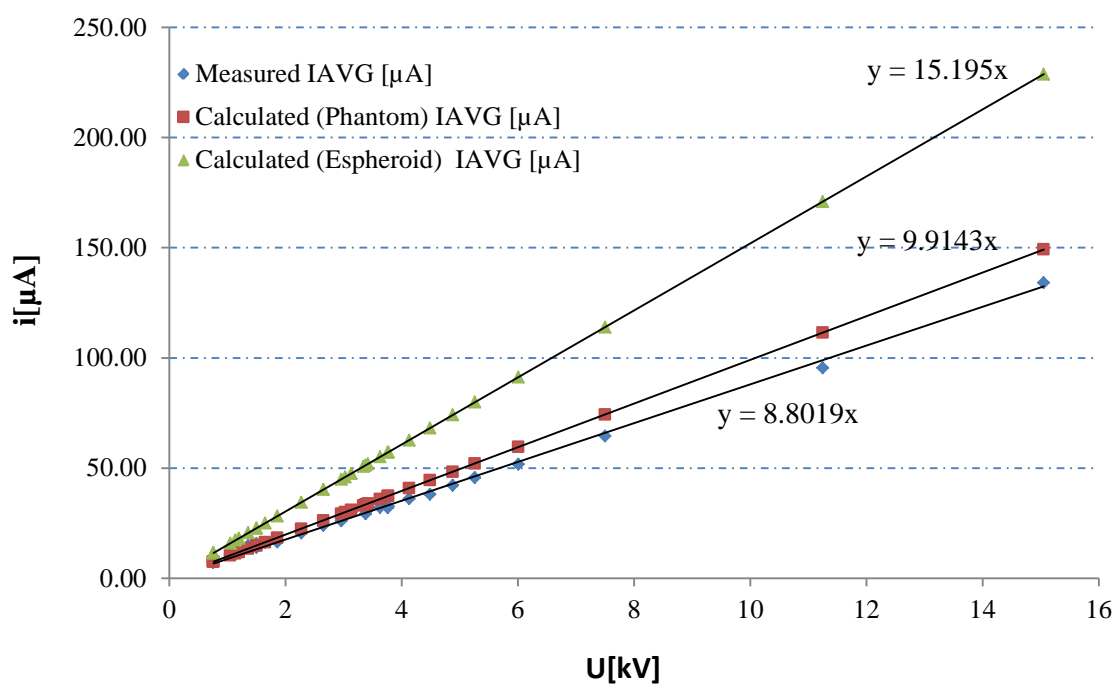
Figure 6.11. *Average of the total induced current (IAVG) as a function of voltage for the lateral configuration.*

The following table represents the values for measurements and calculations for the front configuration.

Table 6.2. *Values obtained of induced current within the phantom as a function of voltage. The values were also calculated with models, spherical model and phantom model in the front configuration, and the relative error in percent.*

#	U [kV]	I$_{AVG}$ [μA]			ϵ_r [%]	
		Measured	Calculated		phantom	Spheroid
			Phantom	Spheroid		
1	7.54	82.3	89.82	113.97	9.14	38.48
2	11.24	120.5	133.9	170.95	11.12	41.86
3	15.00	160.5	178.69	228.69	11.33	42.49

Again the spheroid model has a very high relative error, on average have 40.94%. This is because the surface exposed to the electric field is greater than in the actual case. We say that although it is high, the error we make on average is less than the other configuration, because the distance to the positive electrode is the same as in the real case, both have the same width 0.48m (above 0.37) and are centrally located within the parallel plates in this configuration this model is still insufficient for obtaining an accurate value of the total induced current.

The phantom model presents a relative error of 10.53%. This error is of the same order as above, and is slightly higher than the real case for the same reason that the lateral configuration.

If we represent, as in the previous case, the total induced current versus voltage, see Figure 6.12, we see that there is a proportionality between the total current and the voltage, as expected to happen.
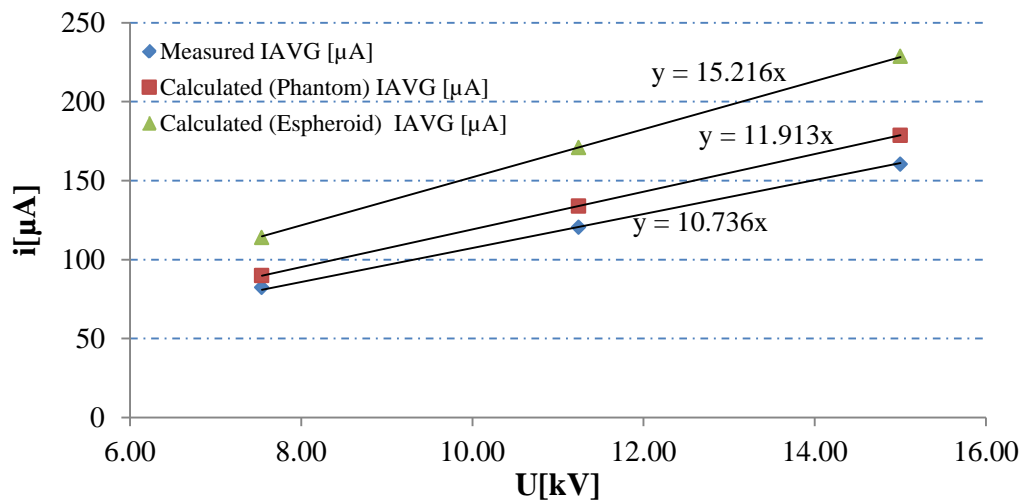
Figure 6.12. *Average of the total induced current (IAVG) as a function of voltage for the frontal configuration.*

7. SUMMARY

In order to detect when the ICD receives disturbances, were carried out two days of experiments in the High Voltage laboratory of the Tampere University of Technology, in a controlled climate room. In previous research, our research group (EPR Environmental Health) had detected, that under certain conditions, the ICD receives interferences under the power lines.

In this master thesis, we designed a protocol for carrying out such experiments in the high voltage laboratory. This protocol covers from the preparation before the experiment to its implementation.

From these experiments, we obtained valuable data, which are used to check numerical methods, such as the total induced current inside the phantom as a function of the applied voltage. Furthermore, ICD readings did not give us conclusive information. Because on the first day of the experiments in all readings of the ICD, we found that there had been at least one disturbance. While in the second day, we did not detect any interference. These two values are completely opposite values and we cannot reach definitive conclusions on when and how such interference appears.

Also, we recreated the whole scenario of the experiment in three dimensions, in this scenario the most difficult task was without a doubt recreating the phantom. Also this is the most important part because as demonstrated in this thesis, depending on the shape that the model has, we have acceptable solutions or solutions that differ significantly from the experimental results. To create this model we used SolidWorks 2011, so as to create the parallel plates.

The created model was imported to Comsol Multiphysics 4.2 second, which created the walls of the laboratory and assigned materials for each part. This software uses the FEM technique to solve differential equations related to the phenomenon being studied.

These calculations allowed us to know, magnitudes that are physically impossible to measure, such as the electric field lines within the parallel plates and the equipotential lines.

From the two models designed to emulate the mannequin, the phantom model is far more accurate than the spherical model, because if we compare the worst case, the mean relative error of both is of 10.53% and 63.58% respectively. This allows us to conclude that the spherical model does not allow calculating with accuracy the value of the total induced current, while the phantom model does although it can be improved.

One of the possible improvements that can be made to this model is to perform surface cuts on his hands, in order to give it a more realistic model-like, or to create a model of separate pieces that could be assembled later.

In future researches, it could create a model of an ICD and then include it inside the phantom, allowing knowing induced electric fields and current densities, inside and nearby these implants in more details when exposed to ELF electric fields.

REFERENCES

[1] B. S. Wilson, C. C. Finley, D. T. Lawson, R. D. Wolford, D. K. Eddington, and W. M. Rabinowitz, "Better speech recognition with cochlear implants," *Nature*, vol. 352, pp. 236-238, 1991.

[2] E. Zrenner, "Will retinal implants restore vision?," *Science*, vol. 295, no. 5557, pp. 1022-1025, 2002.

[3] S. C. Jacobsen, D. F. Knutti, R. T. Johnson, and H. H. Sears, "Development of the Utah artificial arm.," *IEEE Transactions on Biomedical Engineering*, vol. 29, no. 4, pp. 249-269, 1982.

[4] Q. Liu, H. Cai, Y. Xu, Y. Li, R. Li, and P. Wang, "Olfactory cell-based biosensor: a first step towards a neurochip of bioelectronic nose.," *Biosensors and Bioelectronics*, vol. 22, no. 2, pp. 318-322, 2006.

[5] K. L. Kroeker, "Engineering sensation in artificial limbs," *Communications of the ACM*, vol. 54, no. 4, p. 16, 2011.

[6] R. B. North, D. H. Kidd, M. Zahurak, C. S. James, and D. M. Long, "Spinal cord stimulation for chronic, intractable pain: experience over two decades.," *Neurosurgery*, vol. 32, no. 3. pp. 384-394; discussion 394-395, 1993.

[7] C. Marschilok, "Update on insulin pump therapy.," *School Nurse News*, vol. 21, no. 2, pp. 12-13, 2007.

[8] F. Coltorti et al., "The implantable cardioverter defibrillator.," *Revista portuguesa de cardiologia orgao oficial da Sociedade Portuguesa de Cardiologia Portuguese journal of cardiology an official journal of the Portuguese Society of Cardiology*, vol. 357, no. 9262, pp. 1107-1117, 2002.

[9] L. Korpinen, H. Kuisti, J. Elovaara, and V. Virtanen, "Cardiac Pacemakers in Electric and Magnetic Fields of 400-kV Power Lines," *Pace (In press)*. 2012.

[10] Mcdaniel and D. D. Orazio, "Remote Management of Cardiac Patients: The Forefront of a New Standard," *Modern Healthcare*, 2011.

[11] ICNIRP, "Guidelines for Limiting Exposure to Time-Varying Electric and Magnetic Fields (1Hz to 100 KHz): Erratum.," in *Health Physics*, vol. 99, no. 1, 2010, p. 112.

[12] D. Deno and L. Zaffanella, *Field effects of overhead transmission lines and stations. In transmission line reference book-345 and above*. 1982, pp. 329-420.

[13] O. P. Gandhi and J. Y. Chen, "Numerical dosimetry at power-line frequencies using anatomically based models.," *Bioelectromagnetics*, vol. 1, no. 1 & 992, pp. 43-60, 1992.

[14] O. P. Gandhi, G. Kang, D. Wu, and G. Lazzi, "Currents induced in anatomic models of the human for uniform and nonuniform power frequency magnetic fields.," *Bioelectromagnetics*, vol. 22, no. 2, pp. 112-121, 2001.

[15] T. W. Dawson, K. Caputa, and M. A. Stuchly, "High-resolution organ dosimetry for human exposure to low-frequency electric fields," *IEEE Transactions on Power Delivery*, vol. 13, no. 2, pp. 366-373, 1998.

[16] T. W. Dawson, K. Caputa, and M. A. Stuchly, "Electric fields induced in humans and rodents by 60 Hz magnetic fields.," *Physics in Medicine and Biology*, vol. 47, no. 14, pp. 2561-2568, 2002.

[17] A. Christ et al., "The Virtual Family--development of surface-based anatomical models of two adults and two children for dosimetric simulations.," *Physics in Medicine and Biology*, vol. 55, no. 2, p. N23-N38, 2010.

[18] A. M. Katz, *Physiology of the Heart*. Lippincott Williams & Wilkins, 2010, p. 576.

[19] J. E. Hall and A. C. Guyton, *Guyton and Hall textbook of medical physiology*. Saunders/Elsevier, 2010, p. 1091.

[20] B. M. Koeppen and B. A. Stanton, *Berne & Levy Physiology, Updated Edition, 6th Edition*. Elsevier, 2010, p. 848.

[21] M. Prives, N. Lisenkov, and V. Bushkovich, *Anatomía humana, Volume 3*. Mir, 1989.

[22] I. E. Alcamo, P. Review, and J. Bergdahl, *Anatomy Coloring Workbook*. The Princeton Review, 2003, p. 304.

[23] P. A. Iaizzo, *Handbook of Cardiac Anatomy, Physiology, and Devices*. Springer, 2009, p. 659.

[24] R. R. Goderich, *Temas de Medicina Interna*, vol. I. ECIMED, 2002.

[25] A. S. Fauci et al., *Harrison Principios de Medicina Interna*, 17th ed. McGraw-Hill, 2005, p. 3484.

[26] M. Glikson et al., "Are routine arrhythmia inductions necessary in patients with pectoral implantable cardioverter defibrillators?," *Journal of Cardiovascular Electrophysiology*, vol. 11, no. 2, pp. 127-135, 2000.

[27] A. Bhatia et al., "The implantable cardioverter defibrillator: technology, indications, and impact on cardiovascular survival.," *Current Problems in Cardiology*, vol. 29, no. 6, pp. 303-356, 2004.

[28] J. Väisänen, J. Requena-Carrión, F. Alonso-Atienza, J. L. Rojo-Alvarez, J. Malmivuo, and J. Hyttinen, "Contribution of the left anterior myocardium to the body surface potentials in case of apical ectopic beat.," *Conference Proceedings of the International Conference of IEEE Engineering in Medicine and Biology Society*, vol. 2007, pp. 931-934, 2007.

[29] M. W. Kroll and M. H. Lehmann, *Implantable Cardioverter Defibrillator Therapy: The Engineering-Clinical Interface (Developments in Cardiovascular Medicine)*. Springer, 1996, p. 608.

[30] R. X. Stroobandt, S. S. Barold, and A. F. Sinnaeve, *Implantable Cardioverter - Defibrillators Step by Step: An Illustrated Guide*. Wiley-Blackwell, 2009, p. 440.

[31] S. Tanaka, "An overview of the fifth-generation implantable cardioverter defibrillator. [Review] [56 refs]," *Annals of Thoracic Cardiovascular Surgery*, vol. 4, no. 6, pp. 303-311, 1998.

[32] L. D. Lynd and B. J. O'Brien, "Cost-effectiveness of the implantable cardioverter defibrillator: a review of current evidence," *J Cardiovasc Electrophysiol*, vol. 14, no. 9, pp. S99-103, 2003.

[33] P. Mason and C. McPherson, "Implantable cardioverter defibrillator: a review. [Review]," *Heart Lung*, vol. 21, no. 2, pp. 141-147, 1992.

[34] D. Halperin et al., "Pacemakers and Implantable Cardiac Defibrillators: Software Radio Attacks and Zero-Power Defenses," *2008 IEEE Symposium on Security and Privacy sp 2008*, vol. 17, no. 1, pp. 129-142, 2008.

[35] J. D. Causey, H. C. Schioss, and J. D. Snell, "United States Patent," U.S. Patent 4,809,6971989.

[36] A. W. C. Chow and A. E. Buxton, *Implantable Cardiac Pacemakers and Defibrillators: All You Wanted to Know*. BMJ Books, 2006, p. 184.

[37] Y. Rahmat-Samii and J. Kim, *Implanted antennas in medical wireless communications*. Morgan & Claypool Publishers, 2006, p. 76.

[38] J. W. Poore, E. Falkenberg, and G. A. Barazin, "Combined programming wand and psa for pacemaker and icd programmer system," U.S. Patent 7,103,414 B12006.

[39] R. Gradaus, G. Breithardt, and D. Böcker, "ICD leads: design and chronic dysfunctions.," *Pacing and clinical electrophysiology PACE*, vol. 26, no. 2 Pt 1, pp. 649-657, 2003.

[40] A. Saltman, "Clinical Cardiac Pacing and Defibrillation," *Cardiovascular Surgery*, vol. 9, no. 5, pp. 517-518, 2001.

[41] D. J. Lang, J. E. Heil, S. J. Hahn, C. C. Lindstrom, and D. L. Derfus, "Implantable cardioverter defibrillator lead technology: improved performance and lower defibrillation thresholds.," *Pacing and clinical electrophysiology PACE*, vol. 18, no. 3 Pt 2, pp. 548-559, 1995.

[42] D. K. Cheng, *Field and wave electromagnetics*. Addison-Wesley, 1989, p. 703.

[43] J. R. Reitz, F. J. Milford, and R. W. Christy, *Foundations of electromagnetic theory*. Pearson/Addison-Wesley, 2008, p. 630.

[44] R. K. Wangsness, *Electromagnetic fields*. Wiley, 1986, p. 587.

[45] A. Kovetz, *The principles of electromagnetic theory*. CUP Archive, 1990, p. 221.

[46] J.-M. Jin, *The finite element method in electromagnetics*. Wiley, 1993, p. 442.

[47] J.-M. Jin, *Theory and Computation of Electromagnetic Fields*, vol. 2010. John Wiley & Sons, 2010, p. 600.

[48] E. J. Rothwell and M. J. Cloud, *Electromagnetics*. CRC Press, 2008, p. 704.

[49] L. Hoang and R. Scorretti, "Induced current into the human body by power frequency electric and magnetic fields," *Bioelectromagnetism*.

[50] S. W. Min, E. S. Kim, and S. H. Myung, "Calculation and Measurement of Induced Current Density Inside Human Body Under 60 Hz ELF Magnetic Fields," in *IEICE*, 2009, pp. 185-188.

[51] C. Peratta and A. Peratta, *Modelling the human body exposure to ELF electric fields*. WIT Press, 2010, p. 130.

[52] M. Annila, "Sydämentahdistimien ja rytmihäiriötahdistimien häiriintymisen mittaaminen voimajohdon alla," 2010.

[53] M. Wirta, "Pientaajuisten sähkökenttämittausten toistettavuuden parantaminen," 2011.

[54] O. C. Zienkiewicz, R. L. Taylor, R. L. Taylor, and J. Z. Zhu, *The finite element method: its basis and fundamentals*. Butterworth-Heinemann, 2005, p. 733.

[55] B. Wah, "Finite element method," *Wiley Encyclopedia of Computer Science and Engineering*, pp. 1-12, 2008.

[56] D. W. Pepper and J. C. Heinrich, *The finite element method: basic concepts and applications, Volume 1*. Taylor & Francis, 1992, p. 240.

[57] H. Tarao, L. Korpinen, J. Elovaara, H. Kuisti, N. Hayashi, and K. Isaka, "Numerical Evaluation of Currents Induced in a Worker by ELF Non-Uniform Electric Fields in High Voltage Substations and Comparison of them with Experimental Results.," *Bioelectromagnetics (Submitted)*, 2012.

[58] Y. Shiau and A. R. Valentino, "ELF electric field coupling to dielectric spheroidal models of biological objects.," *IEEE Transactions on Biomedical Engineering*, vol. 28, no. 6, pp. 429-437, 1981.

APPENDIX I. Arrhythmias
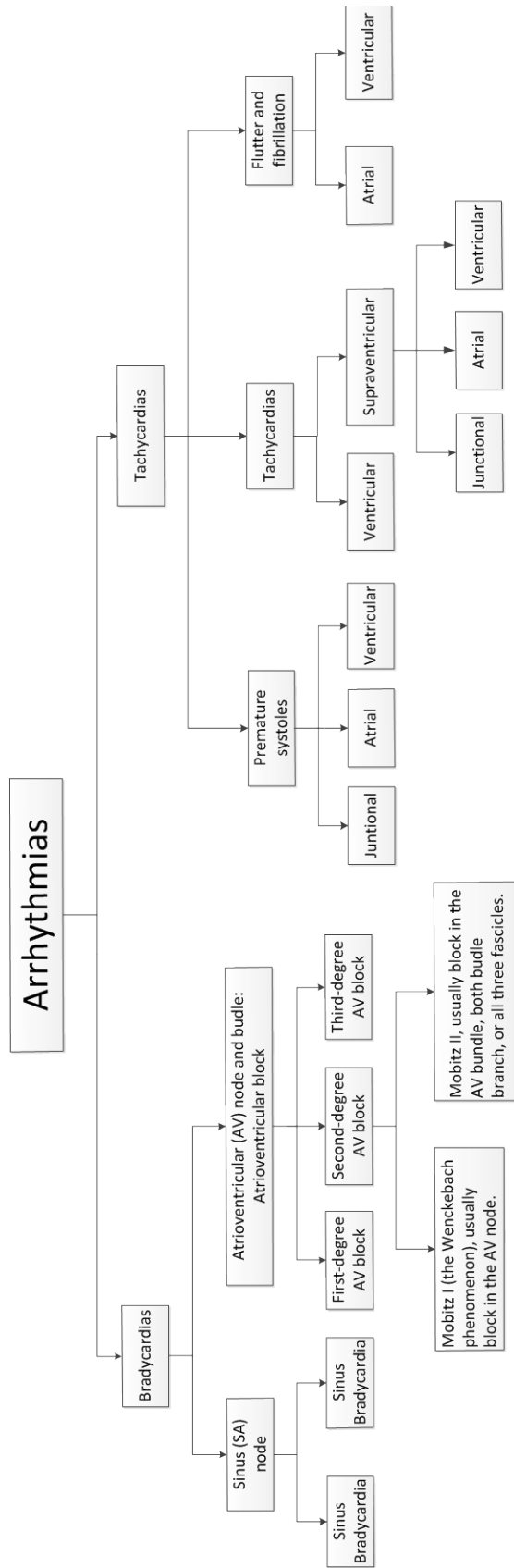
Figure 1. Classification of the arrhythmias [19-22].

APPENDIX II. First day of the experiments.

Place:	High Voltage Lab. (TUT)		First step of the protocol	
Date:	04.10.2011		Start time:	08:52
Measurer(s):	González,	Jarold	Finishing time:	17:43
	Haapala,	Tero	Start Elec. Field[1]:	643 mV/m
	Korpinen,	Leena	Start Temperature[2]:	20.4 ^{0}C
	Tarao,	Hiroo	Start Humidity[3]:	41.8 %
[1] **EFA-300 Field Analyzer**				
[2,3] **Climate room meter**				

Table 1. *Verification of the separation between plates of the experiment. First step.*

#	Meter	Humidity	Temperature	Voltage	Calculated Field	Measured field	Relative Error
		[%]	[^{0}C]	[kV]	[kV/m]	[kV/m]	[%]
1	EFA-300	41.8	20.4	0.76	1.013	1.011	0.23
2	EFA-300	41.7	20.4	1.50	2.000	1.993	0.35
3	EFA-300	41.7	20.4	2.23	2.973	2.959	0.48
4	EFA-300	41.7	20.4	2.98	3.973	3.960	0.34
5	EFA-300	41.7	20.4	3.72	4.960	4.937	0.46
6	EFA-300	41.7	20.4	4.50	6.000	6.017	0.28
7	EFA-300	41.7	20.4	5.26	7.013	7.032	0.27
8	EFA-300	41.7	20.4	6.01	8.013	8.036	0.28
9	EFA-300	41.7	20.4	6.74	8.987	9.008	0.24
10	EFA-300	41.7	20.4	7.51	10.013	10.030	0.17
11	EFA-300	41.7	20.4	8.26	11.013	11.030	0.15
12	EFA-300	41.7	20.4	8.98	11.973	12.000	0.22
13	EFA-300	41.7	20.5	9.76	13.013	13.040	0.20
14	EFA-300	41.6	20.6	10.27	13.693	13.720	0.19
15	EFA-300	41.5	20.5	10.99	14.653	14.680	0.18
16	EFA-300	41.5	20.5	11.78	15.707	15.720	0.08
17	EFA-300	41.4	20.6	12.51	16.680	16.660	0.12
18	EFA-300	41.4	20.6	13.23	17.640	17.580	0.34
19	EFA-300	41.4	20.6	14.00	18.667	18.640	0.14
20	EFA-300	41.4	20.6	14.74	19.653	19.640	0.07
21	EFA-300	41.4	20.6	18.74	24.987	24.950	0.15
22	EFA-300	41.4	20.6	22.52	30.027	30.00	0.09
23	EFA-300	41.4	20.6	26.22	34.960	34.920	0.11
24	EFA-300	41.4	20.6	29.98	39.973	39.950	0.06
25	EFA-300	41.4	20.6	33.74	44.987	44.910	0.17
26	EFA-300	41.4	20.6	37.51	50.013	49.900	0.23

Table 2. *Compilation of all data obtained in the laboratory. First day.*

#		Time	ICD#	Room Parameters		Electric Field			Current			Water		Time	ICD read		Time
				T [°C]	H [%]	U [kV]	E Exp. [kV/m]	d [m]	I_MIN [µA]	I_MAX [µA]	I_AVG [µA]	σ [mS/cm]	T [°C]		# Episode (s)	Type of Episode	
1	Start	10:30		21.7		0.76			7.1			2.02		10:38	1		10:26
	End	10:35	9		42.2		1.01			7.4			20.5	10:39		T	
								0.75			7.25						
2	Start	10:48		21.7		3.76			31.8			2.09		10:54	1		10:50
	End	10:53	9		42.2		5.01			32.1			21	10:55		T	
								0.75			32.0						
3	Start	11:11		22.3		3.63			32.1			2.06		11:19	1		11:13
	End	11:16	9		42.9		4.84			32.2			21	11:20		T	
								0.75			32.2						
4	Start	11:30		22.6		3.42			31			2.09		11:37	1		11:32
	End	11:35	9		42.5		4.56			31.3			21	11:38		T	
								0.75			31.2						
5	Start	11:47		22.7		3.34			31.6			2.08		11:54	1		11:49
	End	11:52	9		41.8		4.45			32			21	11:55		T	
								0.75			31.8						
6	Start	12:04		22.9		3.13			30.1			2.09		12:11	1		12:05
	End	12:09	9		41.7		4.17			30.2			21	12:12		T	
								0.75			30.2						
7	Start	12:21		23.1		3.03			29.3			2.1		12:27	1		12:23
	End	12:26	9		41		4.04			29.7			21	12:28		T	
								0.75			29.5						
8	Start	12:46		23.2		1.5			15.6			2.1		12:52	1		12:42
	End	12:51	9		40.4		2.00			16			21.5	12:53		T	
								0.75			15.8						

65

Table 2 (*Continuation*)

#		Time	ICD#	Room Parameters		Electric Field		Current		Water		Time	ICD read		Time
9	Start	13:01	9	T [°C]	23.4	U [kV]	2.25	I_MIN [µA]	-	σ [mS/cm]	2.12	13:47	# Episode (s)	1	13:03
	End	13:45		H [%]	39.3	E Exp. [kV/m]	3.00	I_MAX [µA]	-	T [°C]	22.1	13:53	Type of Episode	T	
						d [m]	0.75	I_AVG [µA]	-						
10	Start	14:01	9	T [°C]	23.6	U [kV]	1.65	I_MIN [µA]	16.3	σ [mS/cm]	2.11		# Episode (s)	1	14:02
	End	14:06		H [%]	41.6	E Exp. [kV/m]	2.20	I_MAX [µA]	16.4	T [°C]	22.3		Type of Episode	T	
						d [m]	0.75	I_AVG [µA]	16.4						
11	Start	14:21	9	T [°C]	23.2	U [kV]	1.36	I_MIN [µA]	15.2	σ [mS/cm]	2.11	14:28	# Episode (s)	1	14:24
	End	14:26		H [%]	35.8	E Exp. [kV/m]	1.81	I_MAX [µA]	14.6	T [°C]	22.3	14:29	Type of Episode	T	
						d [m]	0.75	I_AVG [µA]	14.9						
12	Start	14:38	9	T [°C]	23.6	U [kV]	1.2	I_MIN [µA]	12.5	σ [mS/cm]	2.14	14:46	# Episode (s)	1	14:40
	End	14:43		H [%]	37.7	E Exp. [kV/m]	1.60	I_MAX [µA]	12.7	T [°C]	22.5	14:47	Type of Episode	T	
						d [m]	0.75	I_AVG [µA]	12.6						
13	Start	14:57	9	T [°C]	23.9	U [kV]	1.05	I_MIN [µA]	11.2	σ [mS/cm]	2.09	15:03	# Episode(s)	1	14:59
	End	15:02		H [%]	38.6	E Exp. [kV/m]	1.40	I_MAX [µA]	11.1	T [°C]	22.5	15:04	Type of Episode	T	
						d [m]	0.75	I_AVG [µA]	11.2						
14	Start	15:16	9	T [°C]	24	U [kV]	0.76	I_MIN [µA]	8.4	σ [mS/cm]	2.12	15:23	# Episode (s)	1	15:16
	End	15:21		H [%]	39.4	E Exp. [kV/m]	1.01	I_MAX [µA]	8.8	T [°C]	22.5	15:23	Type of Episode	T	15:18
						d [m]	0.75	I_AVG [µA]	8.6						
15	Start	15:41	9	T [°C]	24.2	U [kV]	0.39	I_MIN [µA]	7.3	σ [mS/cm]	2.11	15:48	# Episode (s)	1	15:33
	End	15:46		H [%]	39.4	E Exp. [kV/m]	0.52	I_MAX [µA]	9	T [°C]	22.8	15:49	Type of Episode	T	15:44
						d [m]	0.75	I_AVG [µA]	8.15						

Table 3 *Verification of the separation between plates of the experiment. Last step.*

#	Meter	Humidity	Temperature	Voltage	Calc. E. Field	Measured field	Relative Error
		[%]	[^{0}C]	[kV]	[kV/m]	[kV/m]	[%]
1	EFA-300	32.6	22.7	0.76	1.013	1.007	0.63
2	EFA-300	32.6	22.7	1.50	2.000	1.992	0.40
3	EFA-300	32.6	22.8	2.27	3.027	3.027	0.01
4	EFA-300	32.6	22.8	3.04	4.053	4.040	0.33
5	EFA-300	32.6	22.8	3.78	5.040	5.020	0.40
6	EFA-300	32.6	22.8	4.52	6.027	6.024	0.04
7	EFA-300	32.6	22.8	5.26	7.013	7.020	0.10
8	EFA-300	32.6	22.8	5.98	7.973	7.980	0.08
9	EFA-300	32.6	22.8	6.63	8.840	8.980	1.58
10	EFA-300	32.6	22.8	7.50	10.000	10.030	0.30
11	EFA-300	32.6	22.8	8.26	11.013	11.040	0.24
12	EFA-300	32.6	22.8	9.00	12.000	12.030	0.25
13	EFA-300	32.6	22.8	9.78	13.040	13.080	0.31
14	EFA-300	32.6	22.8	10.78	14.373	13.730	4.48
15	EFA-300	32.6	22.8	10.96	14.613	14.600	0.09
16	EFA-300	32.6	22.9	11.74	15.653	15.680	0.17
17	EFA-300	32.6	22.9	12.51	16.680	16.680	0.00
18	EFA-300	32.7	22.9	13.23	17.640	17.570	0.40
19	EFA-300	32.7	22.9	14.00	18.667	18.640	0.14
20	EFA-300	32.7	22.9	14.78	19.707	19.670	0.19
21	EFA-300	32.7	22.9	18.79	25.053	25.030	0.09
22	EFA-300	32.7	22.9	22.5	30.000	29.930	0.23
23	EFA-300	32.7	22.9	26.21	34.947	34.850	0.28
24	EFA-300	32.7	22.9	30.00	40.000	39.910	0.23
25	EFA-300	32.7	22.9	33.76	45.013	44.930	0.19
26	EFA-300	32.7	22.9	37.50	50.000	49.880	0.24

APPENDIX III. Second day of the experiments.

Place:	High Voltage Lab. (TUT)		First step of the protocol	
Date:	07.10.2011		Start time:	08:26
Measurer(s):	González,	Jarold	Finishing time:	17:43
	Haapala,	Tero	Start Elec. Field[1]:	685 mV/m
	Korpinen,	Leena	Start Temperature[2]:	20.9 [0]C
	Tarao,	Hiroo	Start Humidity[3]:	35.9 %
[1] **EFA-300 Field Analyzer**				
[2,3] **Climate room meter**				

Table 1 *Verification of the separation between plates of the experiment. First step*

#	Time	Meter	Humidity	Temperature	Voltage	Calculated Field	Measured Field	Relative Error
			[%]	[ºC]	[kV]	[kV/m]	[kV/m]	[%]
1	8:26	EFA-300	35.9	20.9	0.75	1.000	1.002	0.20
2	8:27	EFA-300	35.8	20.9	1.45	1.933	1.940	0.34
3	8:28	EFA-300	35.8	21	2.26	3.013	3.055	1.38
4	8:29	EFA-300	35.8	21	3.03	4.040	4.052	0.30
5	8:30	EFA-300	35.8	21	3.76	5.013	4.993	0.41
6	8:31	EFA-300	35.8	21	4.50	6.000	6.034	0.57
7	8:32	EFA-300	35.8	21.1	5.25	7.000	7.037	0.53
8	8:33	EFA-300	35.7	21.1	6.04	8.053	8.083	0.37
9	8:34	EFA-300	35.7	21.1	6.71	8.947	8.994	0.53
10	8:35	EFA-300	35.7	21.2	7.46	9.947	10.010	0.64
11	8:36	EFA-300	35.7	21.2	8.25	11.000	11.070	0.64
12	8:37	EFA-300	35.7	21.2	9.04	12.053	12.110	0.47
13	8:38	EFA-300	35.7	21.2	9.82	13.093	13.150	0.43
14	8:40	EFA-300	35.7	21.2	10.49	13.987	14.040	0.38
15	8:41	EFA-300	35.7	21.2	11.27	15.027	15.120	0.62
16	8:41	EFA-300	35.7	21.2	11.97	15.960	16.020	0.38
17	8:42	EFA-300	35.7	21.2	12.71	16.947	17.010	0.37
18	8:43	EFA-300	35.7	21.2	13.57	18.093	18.050	0.24
19	8:44	EFA-300	35.7	21.2	14.28	19.040	19.070	0.16
20	8:45	EFA-300	35.7	21.2	14.98	19.973	20.020	0.23
21	8:46	EFA-300	35.7	21.2	18.74	24.987	25.050	0.25
22	8:47	EFA-300	35.7	21.2	22.54	30.053	30.110	0.19
23	8:48	EFA-300	35.7	21.2	26.26	35.013	35.080	0.19
24	8:49	EFA-300	35.7	21.2	30.05	40.067	40.130	0.16
25	8:49	EFA-300	35.7	21.2	33.74	44.987	45.050	0.14
26	8:49	EFA-300	35.7	21.2	37.49	49.987	50.090	0.21

Table 2 *Compilation of all data obtained in the laboratory. Second day.*

#	Time Start	Time End	ICD#	T [°C]	H [%]	U [kV]	E Exp. [kV/m]	d [m]	I_{MIN} [μA]	I_{MAX} [μA]	I_{AVG} [μA]	σ [mS/cm]	Water T [°C]	Time	Time	# Episode (s)	Type of Episode
1	9:46	9:52	2	21.9	37	0.76	1.01	0.75	7.3	7.8	7.6	-	-	-	-		
2	9:52	9:57	2	22	36.7	0.76	1.01	0.75	7	7.8	7.4	2.15	21.8	9:59	9:59	0	
3	10:08	10:13	2	22.5	37.1	1.14	1.52	0.75	10.7	11.2	11.0	2.2	21.8	10:14	10:15	0	
4	10:21	10:26	2	22.8	36.7	1.5	2.00	0.75	13.8	14.3	14.05	2.19	21.9	10:14	10:15	0	
5	10:34	10:39	2	22.9	37.2	1.86	2.48	0.75	16.4	16.6	16.5	2.16	21.9	10:40	10:41	0	
6	10:48	10:53	2	23.1	37.1	2.27	3.03	0.75	20.3	20.8	20.55	2.18	22.3	10:54	10:54	0	
7	11:01	11:06	2	23.4	37.2	2.65	3.53	0.75	23.7	24.4	24.1	2.14	22.2	11:07	11:08	0	

Table 2 (Continuation)

#		Time	ICD#	Room Parameters		Electric Field		Current		Water		Time	ICD read	Time
8	Start	11:20		T [°C]	23.5	U [kV]	2.96	I_{MIN} [μA]	25.7	σ [mS/cm]	2.16	11:26	# Episode (s)	0
	End	11:25	2	H [%]	36.8	E Exp. [kV/m]	3.95	I_{MAX} [μA]	26.4	T [°C]	22.5	11:27	Type of Episode	
						d [m]	0.75	I_{AVG} [μA]	26.05					
9	Start	11:33		T [°C]	23.6	U [kV]	3.38	I_{MIN} [μA]	28.9	σ [mS/cm]	2.18	11:39	# Episode (s)	0
	End	11:38	2	H [%]	36.3	E Exp. [kV/m]	4.51	I_{MAX} [μA]	29.6	T [°C]	22.6	11:40	Type of Episode	
						d [m]	0.75	I_{AVG} [μA]	29.3					
10	Start	11:48		T [°C]	23.7	U [kV]	3.77	I_{MIN} [μA]	31.6	σ [mS/cm]	2.17	11:54	# Episode (s)	0
	End	11:53	2	H [%]	35.8	E Exp. [kV/m]	5.03	I_{MAX} [μA]	33.6	T [°C]	22.6	11:55	Type of Episode	
						d [m]	0.75	I_{AVG} [μA]	32.6					
11	Start	12:01		T [°C]	23.8	U [kV]	4.13	I_{MIN} [μA]	35.7	σ [mS/cm]	2.18	12:07	# Episode (s)	0
	End	12:06	2	H [%]	35.3	E Exp. [kV/m]	5.51	I_{MAX} [μA]	36.6	T [°C]	22.7	12:08	Type of Episode	
						d [m]	0.75	I_{AVG} [μA]	36.2					
12	Start	12:13		T [°C]	23.9	U [kV]	4.49	I_{MIN} [μA]	37.9	σ [mS/cm]	2.16	12:19	# Episode (s)	0
	End	12:18	2	H [%]	34.8	E Exp. [kV/m]	5.99	I_{MAX} [μA]	38.5	T [°C]	22.9	12:20	Type of Episode	
						d [m]	0.75	I_{AVG} [μA]	38.2					
13	Start	12:26		T [°C]	23.9	U [kV]	4.88	I_{MIN} [μA]	41.9	σ [mS/cm]	2.19	13:11	# Episode (s)	0
	End	13:09	2	H [%]	34.6	E Exp. [kV/m]	6.51	I_{MAX} [μA]	42.6	T [°C]	23.1	13:12	Type of Episode	
						d [m]	0.75	I_{AVG} [μA]	42.3					
14	Start	13:19		T [°C]	24	U [kV]	5.26	I_{MIN} [μA]	45.1	σ [mS/cm]	2.13	13:25	# Episode (s)	0
	End	13:24	2	H [%]	35.5	E Exp. [kV/m]	7.01	I_{MAX} [μA]	46.4	T [°C]	23.2	13:26	Type of Episode	
						d [m]	0.75	I_{AVG} [μA]	45.75					

70

Table 2 (*Continuation*)

#	Time		ICD#	Room Parameters		Electric Field			Current			Water			Time		ICD read		Time
16	Start	13:45		T [°C]	24.2	U [kV]	7.5	I_MIN [µA]	63.7	σ [mS/cm]	2.16		13:51	# Episode (s)	0				
	End	13:50	2	H [%]	35.4	E Exp. [kV/m]	10.00	I_MAX [µA]	65.6	T [°C]	23.4		13:52	Type of Episode					
						d [m]	0.75	I_AVG [µA]	64.65										
17	Start	13:57		T [°C]	24.4	U [kV]	11.3	I_MIN [µA]	94.6	σ [mS/cm]	2.19		14:03	# Episode (s)	0				
	End	14:02	2	H [%]	35.5	E Exp. [kV/m]	15.00	I_MAX [µA]	96.3	T [°C]	23.2		14:04	Type of Episode					
						d [m]	0.75	I_AVG [µA]	95.5										
18	Start	14:10		T [°C]	24.5	U [kV]	15.1	I_MIN [µA]	133.8	σ [mS/cm]	2.19		14:16	# Episode (s)	0				
	End	14:15	2	H [%]	35.7	E Exp. [kV/m]	20.07	I_MAX [µA]	134.4	T [°C]	23.5		14:17	Type of Episode					
						d [m]	0.75	I_AVG [µA]	134.1										
19	Start	15:01		T [°C]	22.6	U [kV]	7.54	I_MIN [µA]	82.1	σ [mS/cm]	2.18		15:07	# Episode (s)	0				
	End	15:06	2	H [%]	33.3	E Exp. [kV/m]	10.05	I_MAX [µA]	82.4	T [°C]	23		15:08	Type of Episode					
						d [m]	0.75	I_AVG [µA]	82.3										
20	Start	15:13		T [°C]	23.5	U [kV]	11.2	I_MIN [µA]	120	σ [mS/cm]	2.17		15:19	# Episode (s)	0				
	End	15:18	2	H [%]	32.7	E Exp. [kV/m]	14.99	I_MAX [µA]	120.9	T [°C]	23.1		15:20	Type of Episode					
						d [m]	0.75	I_AVG [µA]	120.5										
21	Start	15:25		T [°C]	23.8	U [kV]	15	I_MIN [µA]	160.4	σ [mS/cm]	2.17		15:31	# Episode (s)	0				
	End	15:30	2	H [%]	33.1	E Exp. [kV/m]	20.00	I_MAX [µA]	161	T [°C]	23		15:32	Type of Episode					
						d [m]	0.75	I_AVG [µA]	160.5										

Table 3 *Verification of the separation between plates of the experiment. Last step.*

#	Time	Meter	Humidity	Temperature	Voltage	Calculated Field	Measured Field	Relative Error
			[%]	[ºC]	[kV]	[kV/m]	[kV/m]	[%]
1	16:05	EFA-300	32.6	22.2	0.76	1.013	1.011	0.23
2	16:06	EFA-300	32.5	22.2	3.75	5.000	4.991	0.18
3	16:07	EFA-300	32.4	22.3	7.48	9.973	10.010	0.37
4	16:07	EFA-300	32.4	22.3	11.27	15.027	15.060	0.22
5	16:08	EFA-300	32.3	22.4	15.06	20.080	20.070	0.05
6	16:09	EFA-300	32.4	22.5	18.76	25.013	25.020	0.03